ABSOLUTE QUANTIFICATION OF PHARMACOKINETIC PARAMETERS IN DYNAMIC CONTRAST ENHANCED MAGNETIC RESONANCE IMAGING

by

Jacob U. Fluckiger

A dissertation submitted to the faculty of
The University of Utah
in partial fulfillment of the requirements for the degree of

Doctor of Philosophy

Department of Bioengineering

The University of Utah

May 2011

The University of Utah Graduate School

STATEMENT OF DISSERTATION APPROVAL

The dissertation of **Jacob Fluckiger**

has been approved by the following supervisory committee members:

Edward DiBella	, Chair	**12/9/2010** Date Approved
Rob MacLeod	, Member	**10/5/2010** Date Approved
Edward Hsu	, Member	**10/5/2010** Date Approved
Sarang Joshi	, Member	**10/5/2010** Date Approved
Matthias Schabel	, Member	**10/5/2010** Date Approved

and by **Richard Rabbitt**, Chair of the Department of **Bioengineering**

and by Charles A. Wight, Dean of The Graduate School.

ABSTRACT

We present a method for absolutely quantifying pharmacokinetic parameters in dynamic contrast-enhanced (DCE)-MRI. This method, known as alternating minimization with model (AMM), involves jointly estimating the arterial input function (AIF) and pharmacokinetic parameters from a characteristic set of measured tissue concentration curves. By blindly estimating the AIF, problems associated with AIF measurement in pharmacokinetic modeling, such as signal saturation, flow and partial volume effects, and small arterial lumens can be ignored. The blind estimation method described here introduces a novel functional form for the AIF, which serves to simplify the estimation process and reduce the deleterious effects of noise on the deconvolution process. Computer simulations were undertaken to assess the performance of the estimation process as a function of the input tissue curves. A confidence metric for the estimation quality, based on a linear combination of the SNR and diversity of the input curves, is presented. This confidence metric is then used to allow for localizing the region from which input curves are drawn. Local blood supply to any particular region can then be blindly estimated, along with some measure of confidence for that estimation. Methods for evaluating the utility of the blind estimation algorithm on clinical data are presented, along with preliminary results on quantifying tissue parameters in soft-tissue sarcomas.

The AMM method is applied to *in vivo* data from both cardiac perfusion and breast cancer scans. The cardiac scans were conducted using a dual-bolus protocol, which provides a measure of truth for the AIF. Twenty data sets were processed with this method, and pharmacokinetic parameter values derived from the blind AIF were compared with those derived from the dual-bolus measured AIF. For seventeen of the twenty datasets there were no statistically significant differences in K^{trans} estimates. The cardiac AMM method presented here provides a way to quantify perfusion of myocardial tissue with a single injection of contrast agent and without a special

pulse sequence. The resulting parameters are similar to those given by the dual bolus method. The breast cancer scans were processed with the AMM method and the results were compared to an analysis done with the semiquantitative DCE-MRI scans. The effects of the temporal sampling rate of the data on the AMM method are examined. The ability of the AMM-derived parameters to distinguish benign and malignant tumors is compared to more conventional methods.

To WO, SR and OJ

CONTENTS

LIST OF FIGURES

LIST OF TABLES

ACKNOWLEDGMENTS

I would like to acknowledge the support of Dr. Ed DiBella. Thank you for your time, advice, and assistance. I would also like to thank Dr. Matthias Schabel and the rest of my committee, Drs. Rob Macleod, Edward Hsu, and Sarang Joshi for their help and guidance.

Completing my education would not have been possible without the assistance of my family. Thank you Wendy for putting up with an often absent and stressed husband. Thank you Sophia and Olivia for your smiles and hugs and for reminding me what's most important.

CHAPTER 1

INTRODUCTION

This dissertation aims to address issues in quantitative processing of dynamic contrast enhanced magnetic resonance imaging. Quantitative imaging has the potential to simplify patient diagnosis and aid in developing individual treatment plans for patients suffering from a range of disease.

1.1 Fundamentals of MRI

MRI is an imaging modality that makes use of the principle of magnetic resonance to obtain anatomical and physiological images noninvasively and without the use of ionizing radiation. Since the publication of the first magnetic resonance image in 1973 [**?**], MRI techniques have been developed to image a wide variety of applications including the diffusion of water molecules [**?**, **?**], oxygen dependant brain activity [**?**, **?**] and density and integrity of tissue vasculature [**?**]. The ability of MRI to acquire images in arbitrary imaging planes and with a wide variety of contrast sources makes it an increasingly used clinical tool for diagnosing and monitoring disease.

There are many texts covering the basic principles of magnetic resonance and the use of magnetic resonance in imaging in great detail. The interested reader is referred particularly to those by Haacke [**?**] and Liang [**?**]. In general, magnetic resonance images use nuclei with nonzero net spin such as 1H, 23Na, and 31P among others. The work in this dissertation is concerned solely with the imaging of hydrogen nuclei (or protons) found throughout the body. For more information on nonhydrogen imaging the reader is referred to [**?**].

The proton that composes a hydrogen nucleus has a net magnetic moment with two possible spin states (often referred to as up or down). When placed in a large, uniform, external magnetic field, such as that found in the bore of an MR scanner, the nuclei will experience a torque causing them to align their spin states such that they

precess around the axis of the external field. Due to the differences in energy between the up and down spin states, a slightly larger percentage of the total nuclei will align in the lower energy state, resulting in a net longitudinal magnetization within the body. RF energy, tuned to the characteristic frequency of the spin precession, can then be applied, which results in tipping these spins off the axis of the main magnetic field. Following the application of an RF pulse, the spinning nuclei will regain their initial energy state. The RF energy emitted during this relaxation is the signal recorded by the MR scanner. This signal depends on the density of the nuclei, as well as the interactions among the nuclei as they relax. The characteristic time following the application of an RF pulse during which the net longitudinal magnetization is recovering is known as the longitudinal or spin-lattice relaxation time, T1. The value of T1 for a given proton depends on the local interactions between the hydrogen nuclei. The majority of the hydrogen nuclei in the body are part of water molecules. Pure water has a T1 of several seconds. The interaction of the water with proteins and other biomolecules lowers the T1 in tissue. In general T1 in tissue varies between 100-1000 ms. The differences in T1 among different tissues are a source of contrast in many MRI sequences, including those used in this work.

1.2 Background of DCE-MRI

Dynamic contrast-enhanced imaging methods have been used in a variety of applications and imaging modalities. The main principle behind these methods is the serial acquisition of images of a region of interest before, during and after the injection of a contrast agent. In positron emission tomography (PET) as well as in single photon emission computed tomography (SPECT), contrast injection is a required part of all imaging. In both of these forms of nuclear imaging, the acquired signal comes from the emission of radioactivity from some radiotracer. In static PET or SPECT imaging, the cumulative signal over a period of time is used to reconstruct a single image showing the distribution of the tracer in the subject. By decreasing the amount of time dedicated to each acquisition, an increased number of images can be reconstructed, yielding information on the time course of the tracer distribution. This sort of dynamic imaging has also been applied to x-ray computed tomography

(CT) scanning. In CT imaging, the acquired signal relates to the transmission and attenuation of x-rays through the imaged subject. DCE-CT is possible through the injection of some contrast agent that alters the attenuation properties of the tissue.

The idea of dynamic contrast-enhanced imaging has also been applied to MRI. These methods have been particularly designed to assess the density and permeability of tissue vasculature. DCE-MRI is used primarily to diagnose and monitor diseases where tissue vascularization is a useful biomarker. Two examples of DCE-MRI use in clinical practice are in oncology, and in myocardial perfusion. An example of a DCE-MRI acquisition for myocardial perfusion is seen in Figure 1.1. In oncology, as tumors grow larger than a few mm^3, they are no longer able to meet metabolic

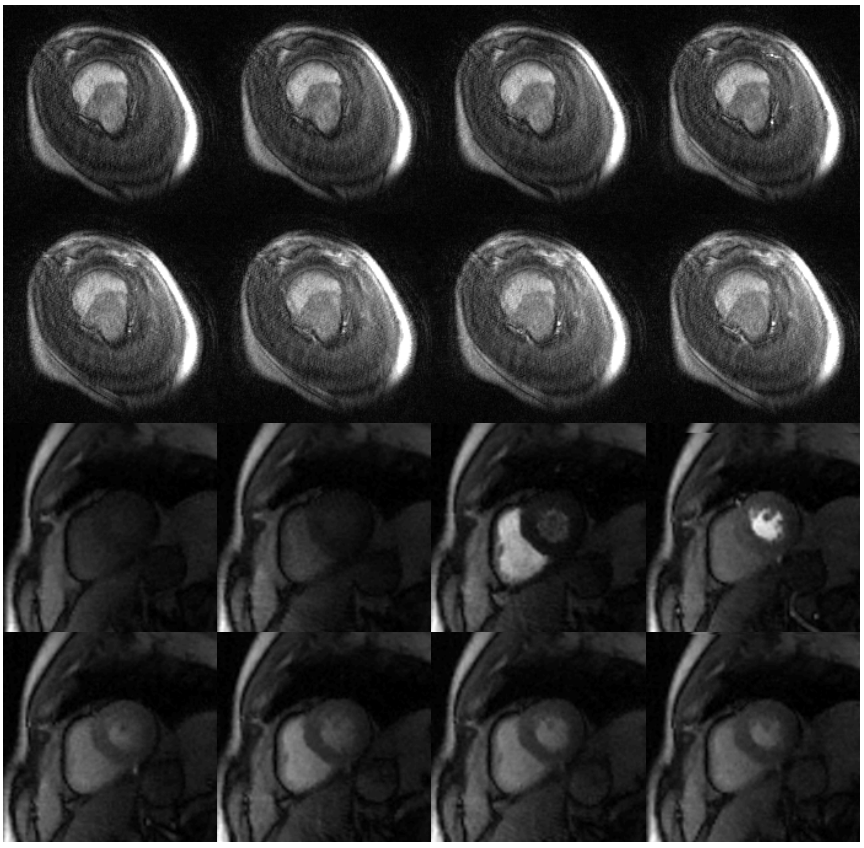

Figure 1.1. Example DCE-MRI scan of a primitive neuroectodermal tumor (PNET) in the distal humerus (first two rows) and a single short axis slice through the heart (second two rows). In the PNET, the contrast can be seen entering the tumor in the upper portion of the image. In the heart, the contrast enters the right ventricle, passing into the left ventricle and then dispersing throughout the blood and tissue.

demands solely through passive diffusion of nutrients. Through a process called angiogenesis, they create new vasculature to supply needed nutrients. These new vessels tend to be very leaky when compared to those in healthy tissue. As a result, DCE-MRI is able to identify tumors based on regions of enhanced leakiness in the vessels. In addition, rapidly growing tumors tend to be very heterogeneous, often having necrotic cores (where cells are no longer able to proliferate) and distinctly active rims with high metabolic activity. In clinical scans, high spatial resolution is often desired to distinguish small tumors from surrounding healthy tissue, as well as to segment larger tumors into regions of high and low activity.

DCE-MRI is also used in myocardial perfusion imaging [**?**, **?**]. In this case, the parameter of greatest interest is the flow of blood to myocardial tissue. Tissue that has been damaged, or tissue that has an inadequate blood supply due to vessel occlusion, are both identifiable in DCE-MRI studies. In these cardiac scans, high temporal resolution is often desirable due to the nature of the kinetics of blood flow through the coronary arteries. In addition, cardiac (and respiratory) motion makes consistent imaging across frames difficult. By imaging the entire region of interest in a short time, greater interframe correlation in cardiac phase is possible.

A separate class of dynamic MRI scans, dynamic contrast susceptibility (DSC) MRI, has also been developed. DSC-MRI is used largely in brain imaging, and differs from DCE-MRI in that DSC studies make use of T2-weighted contrast changes while DCE-MRI studies focus on changes in T1. This work focuses solely on DCE-MRI, the interested reader is referred to [**?**] for more information on DSC-MRI and its applications.

1.3 Principles of DCE-MRI

As stated above, DCE-MRI involves the injection of contrast into the subject to be imaged. Though multiple types of MR contrast exist, this work focuses on the use of paramagnetic gadolinium based chelates. Unlike dynamic CT, PET, or SPECT, DCE-MRI does not measure the concentration of contrast agent directly. Gadolinium ions contain unpaired outer electrons that generate local magnetic fields. These local fields affect the relaxation of hydrogen nuclei and reduce the characteristic relaxation

time. By tracking the change in relaxation over time, the delivery of contrast agent (and the blood supply) can be determined.

The relationship between gadolinium concentration and the relaxation time is often modeled as:

$$\frac{1}{T_1} = \frac{1}{T_{1,0}} + r_1 C \tag{1.1}$$

where r_1 represents the field strength specific relaxivity and C the gadolinium concentration. Similar equations also apply to T2 and T2*. This relationship is within the fast exchange limit, which assumes that the contrast agent and water are well mixed within the time course of the sampling. As described below, the acquired MR signal varies nonlinearly with relaxation times, as a result, the relationship between contrast concentration and MR signal is nonlinear, and saturates at high concentration levels. This nonlinear relationship is illustrated with sample parameters in Figure 1.2. A typical DCE-MRI study involves some measurement of the native (precontrast) T1 values for the region of interest. Following this measurement, T1-weighted images

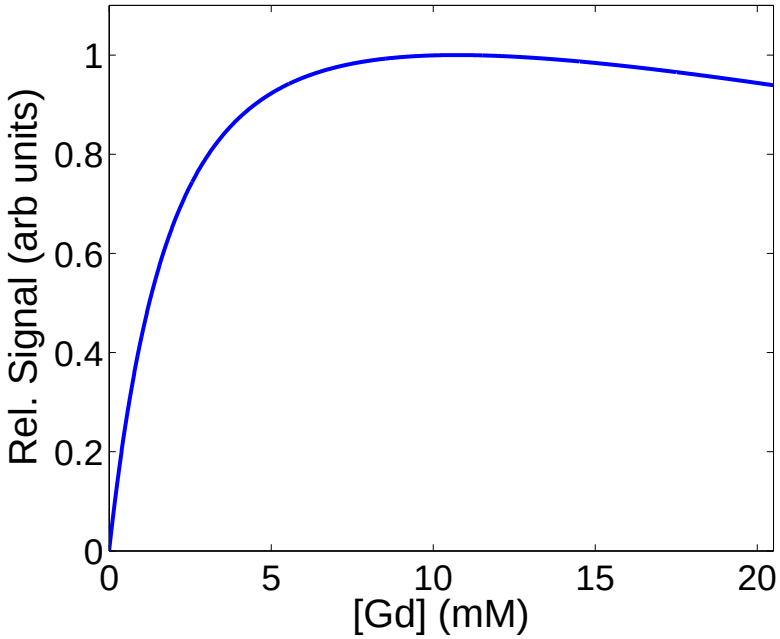

Figure 1.2. The relationship between the relative change in MR signal and the concentration of gadolinium. As the concentration increases, the relationship becomes increasingly nonlinear, and the signal change saturates at high concentrations.

are acquired while a bolus injection of a gadolinium chelate (such as Gadodiamide) is administered. Images are acquired continuously over some predetermined time frame that will depend on the expected kinetics of the contrast agent bolus in the tissue of interest. Depending on the intended use of the data, acquisitions may be focused on obtaining either high spatial resolution (i.e., 0.5mm isotropic) or high temporal resolution (i.e., <15 sec/frame) images. Due to current limitations in scanner hardware and image acquisition and reconstruction, some tradeoff between spatial resolution, temporal resolution and SNR will be made. The details of the acquisition will depend on the intended purpose of the scan. Following acquisition, these images can then be assessed qualitatively, or through the use of quantitative or semiquantitative postprocessing. This work focuses on quantitative processing as described below. For more information on DCE-MRI the reader is referred to [**?**] and the references contained therein.

1.4 Quantitative Postprocessing

Quantitative postprocessing differs from qualitative or semiquantitative processing in that it relies on physical measurements (i.e., T1 values) rather than relative changes in signal intensity (as in semiquantitative analyses). Though more challenging to process, quantitative measurements directly reflect tissue physiology, and are reproducible in different scanning situations.

Quantitative processing begins by converting the acquired MR signal into T1 measurements or contrast agent concentration measurements. This conversion depends on the MR sequence used to acquire the data, and the relaxivity of the contrast agent used. One commonly used family of sequences in oncological DCE-MRI is the gradient echo class, which includes 2D and 3D variants, with a variety of spoiling gradients, balanced gradients and other specialized acquisition techniques. The choice of sequence will depend on the scanner configuration and desired application. In general, the relationship of the acquired signal and the scanning parameters in a standard spoiled gradient echo sequence can be described as

$$S(T_1, T_2^*) = M_0 \frac{\sin(\alpha)(1 - e^{-T_R/T_1})e^{-T_E/T_2^*}}{1 - e^{-T_R/T_1}\cos(\alpha)} \tag{1.2}$$

where M_0 represents a constant signal scale, α represents the flip angle of the pulse sequence, T_R and T_E represent the repetition and echo times of the pulse sequence, and T_1 and T_2^* represent the relaxation times of the tissue [**?**]. As contrast agent enters the tissue of interest, the relative change in signal intensity can be described as

$$\Delta S = \frac{S(T_1, T_2^*) - S(T_{1,0}, T_{2,0}^*)}{S(T_{1,0}, T_{2,0}^*)} \tag{1.3}$$

where the zero subscripts refer to precontrast values. Given the relationship between concentration and T1, equation 1.2 can be solved numerically to obtain a measure of the concentration in that tissue (see [**?**] for a study of the uncertainty and bias in this conversion). Concentration measurements can be obtained voxelwise for each time frame to create tissue concentration time courses for the region of interest.

Saturation recovery sequences are more commonly employed in cardiac DCE-MRI applications. These sequences include one or more pulses prior to the readout of the MRI data. These pulses serve to "saturate" or remove residual longitudinal magnetization prior to the readout. The signal measured during the readout will then depend on some saturation recovery time between the saturation pulse and the readout. As with the gradient echo sequence used in cancer imaging, the change in signal intensity for the saturation recovery sequences varies nonlinearly with contrast concentration. The general signal equation for the n^{th} readout of a saturation recovery sequence is

$$\begin{aligned} S(T_1, T_2^*, n, C) = {} & M_0(\cos(\alpha)e^{-TR/T_1})^{n-1} \\ & \left(e^{-TD/T_1} - \frac{e^{-TR/T_1} - \cos(\alpha)e^{-TR/T_1}}{1 - \cos(\alpha)e^{-TR/T_1}} \frac{1 - e^{-(eSRT - TD)R_1 C}}{1 - e^{-eSRT \cdot R_1 \cdot C}}\right) \\ & (1 - e^{-eSRT \cdot R_1 C}) \end{aligned} \tag{1.4}$$

where $eSRT = TD + (n-1)TR$ is the effective saturation recovery time [**?**]. As with the gradient echo sequence, this equation can be solved numerically to obtain a measure of the concentration in the tissue.

Various mathematical models have been developed to relate the time course of contrast agent to the underlying tissue physiology. The most commonly used model in quantitative DCE-MRI is the two compartment model first developed by Kety [**?**].

Other models, including shutterspeed models [**?**] and adiabatic models [**?**] have also been used; however, this study focuses on the two compartment case.

The two compartment model assumes that the region of interest is composed of two regions, through which contrast agent can travel. These compartments are assumed to be well mixed, in that the water exchange between the intra and extra cellular space is fast compared to the relaxation rate of the water. This is equivalent to treating any contrast agent entering the compartment as immediately distributed uniformly throughout the volume. In DCE-MRI modeling, the first compartment consists of the blood plasma volume fraction (v_p) into which the contrast agent flows. The second compartment is the extracellular, extravascular volume fraction (v_e) (see Figure 1.3). Contrast agent can be exchanged between the two compartments, and the measure of the rates of exchange, as well as the fractional volumes of the two compartments, are the parameters to be measured in this model. The kinetics of the contrast agent in the compartments can be described by the following equations (with derivation and standardized symbols following those given in [**?**]).

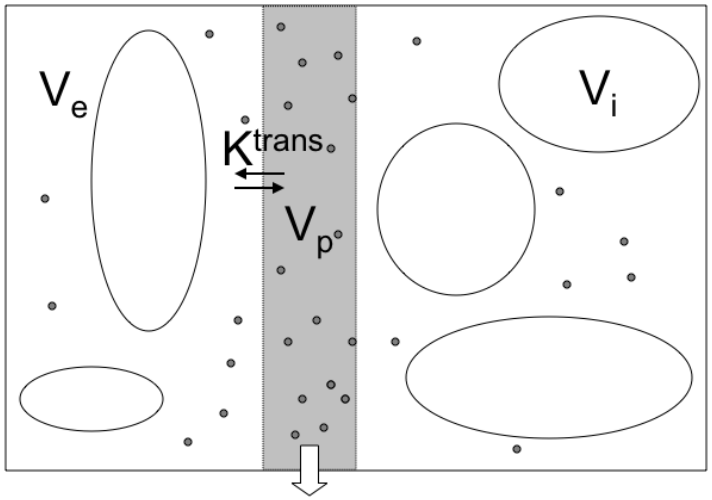

Figure 1.3. Graphical representation of the two compartment model. Blood flows through the region (v_p) allowing the contrast to be exchanged between the two compartments. Current MRI contrast agents do not enter the intracellular space (v_i)

$$\frac{d}{dt}C_t(t) = K^{trans}(C_p - C_t/v_e) = K^{trans}C_p - k_{ep}C_t \tag{1.5}$$

Through the use of appropriate integration constants, equation 1.5 yields the solution

$$C_t(t) = K^{trans}e^{-k_{ep}t} \otimes C_p(t) \tag{1.6}$$

where $\otimes$ represents the convolution operator. It has been noted that equation 1.6, also known as the Kety model, does not explicitly include a plasma compartment. The Kety model can be extended by the inclusion of the plasma compartment to yield the extended Kety model:

$$C_t(t) = K^{trans}e^{-k_{ep}t} \otimes C_p(t) + v_pC_p(t) \tag{1.7}$$

1.5 Arterial Input Functions

Two compartment model parameters are typically found by fitting equation 1.7 to either voxelwise or region averaged (to reduce noise) measured concentration time courses with a nonlinear least squares method. This type of fit requires knowledge of the concentration time course in the blood plasma, also known as the arterial input function (AIF).

The AIF can be measured directly through the use of arterial catheterization. During the contrast injection, samples are drawn directly from the blood supply, and later analyzed chemically to obtain concentration measurements. Though this technique allows for very accurate concentration measurements, the invasive nature of the technique, as well as the relatively poor temporal resolution and added complexity make it less than desirable for regular clinical use.

A second method for determining the AIF makes use of arterial signal within the imaged field of view. Arterial regions of interest are identified (either manually or with computer aided detection) and the signal measurements are converted into concentration in the same manner as the tissue measurements. This method does not require additional imaging, as the AIF and tissue can be gathered simultaneously. Drawbacks to this method include the difficulty of obtaining an accurate arterial signal. In many cases no large arteries are adjacent to the desired field of view, which necessitates an increase in the imaging window with concomitant decreases in

either spatial or temporal resolution. In other cases, the arterial lumens within the field of view are small with respect to the spatial resolution of the image, which results in partial volume effects that must be accounted for in determining the desired AIF [?]. Flow effects may also alter the arterial signal and make accurate concentration measurements difficult to obtain. Lastly, as the concentration of contrast agent in a region increases, the relative change in signal intensity decreases. This signal saturation is especially problematic in the blood plasma, which has higher concentrations of contrast than the surrounding tissue.

Recent work has been done to determine population averaged AIFs [?, ?, ?]. With this method, the same AIF is used for all patients imaged under a particular protocol. Though this method has the advantage of simplicity and ease in calculation, it is unable to account for changes in inter- or intrapatient individuality between scans.

Reference region approaches [?, ?, ?] compare measured values in regions of interest to those from healthy tissue. The parameter values for the healthy, reference tissue are assumed to be consistent with previously reported literature values. Comparing the kinetics of the region of interest to the reference tissue allows for parameter calculation without needing to determine the AIF. These approaches allow for acquisitions with greater focus on spatial resolution at the expense of temporal resolution, as the kinetics of tissues tend to be slower than those for the AIF. However, reference region calculations are limited by the agreement of the parameter values in the tissue to those from literature, and also necessitate the presence of a good reference tissue in the imaging field of view.

In contrast, blind estimation methods like those previously developed for dynamic PET or SPECT [?] and those for DCE-MRI [?, ?, ?] estimate the AIF directly from the tissue concentration time curves. In general, these methods assume that the curves within a region of interest share a common blood input and estimate that input function through statistical methods.

1.6 Scope of Dissertation

The work presented in this dissertation builds upon previously developed blind estimation techniques. Chapter 2 presents the alternating minimization with model

(AMM) method for blindly estimating the AIF. A novel functional form for the AIF is incorporated into the estimation to minimize the effect of noise. Simulations are carried out to assess the benefit of including the AIF model in the estimation and preliminary results from the application of the AMM method to in vivo DCE-MRI data are presented.

Chapter 3 characterizes the performance of the AMM method through monte carlo type computer simulations. The effects of the SNR and diversity among the input tissue curves on the quality of estimation are presented. A metric for estimating the uncertainty in the AMM-estimated AIF is developed. This metric is used to estimate AIFs on small, localized regions of interest within a tumor. The differences between global and local AIF estimation on kinetic parameters in *in vivo* data sets are presented.

The application of the AMM method to myocardial perfusion data sets is presented in Chapter 4. Additional constraints given by the signal in the left ventricular blood pool on the AIF estimation are incorporated into the AMM method to create a cardiac constrained AMM (CAMM) algorithm for use in myocardial perfusion scanning. The results from CAMM-estimated AIFs are compared to the more established dual bolus method in 21 *in vivo* data sets.

Quantitative processing in breast cancer DCE-MRI is presented in Chapter 5. The AMM method is compared to the more commonly used three-time-point semi-quantitative analysis methods. The effects of the temporal sampling rate on both the AMM and three-time-point methods are examined in simulation and with *in vivo* data. The sensitivity and specificity of each of the processing methods are presented.

Chapter 6 discusses the current state of AMM estimation and presents ideas for future research in this area.

CHAPTER 2

MODEL-BASED BLIND ESTIMATION

Portions of this chapter originally appeared in "Model-based blind estimation of kinetic parameters in dynamic contrast enhanced (DCE)-MRI" Mag. Res. Med. Volume 62 Issue 6, Pages 1477 - 1486. Reprinted with permission.

2.1 Introduction

This work focuses on blind estimation techniques for extracting kinetic parameters and AIFs simultaneously from DCE-MRI data that do not require either measured AIF data or statistical estimates of pharmacokinetic parameters in reference tissues. We build on the work reported previously by Riabkov and DiBella [**?**] that used the iterative quadratic maximum likelihood (IQML) algorithm for blind estimation of kinetic parameters, and also on a similar approach by Yang et al. [**?**]. A key difference here is firstly that a novel functional form for the input function, which can accurately model the shape of the AIF while simultaneously minimizing the effect of noise, is introduced. A second important difference in this work is that the characteristics of AIFs that are estimated when arterial voxels are not included in the field of view are studied. That is, blind estimation using time curves from both tissue and arterial voxels provides input functions similar to those measured directly from the arterial voxels. In contrast, when arterial voxels are excluded from the estimation process, with the algorithm based on only tissue curves from a particular region, the resulting input function is dispersed and delayed as compared to the AIF measured in the arterial voxels. This suggests that the true input function seen by tissue voxels is different from that measured in a nearby artery, consistent with the work of Calamante and others on local input functions measured using dynamic susceptibility contrast in the brain [**?**, **?**]. We discuss the mathematical basis of our

algorithm and present preliminary results on both simulated and measured data.

2.2 Materials and Methods

2.2.1 Blind Estimation Analysis

The basic algorithm used here is described in detail in [**?**]. We begin with an extended Tofts-Kety two compartment model for tissue CA concentration:

$$C_t(t) = K^{trans} e^{-k_{ep}t} \otimes C_p(t) + v_p C_p(t) \tag{2.1}$$

where K^{trans} and k_{ep} are the transfer constant and rate constant respectively, $\otimes$ is the convolution operator, v_p is the blood plasma volume fraction, and $C_p(t)$ is the concentration of CA in the blood plasma [**?**]. The blind estimation method takes advantage of the discrete nature of MRI data and creates an objective function:

$$R = ||\vec{C_t}(t) - [H + \Delta]\vec{C_p}(t)|| \tag{2.2}$$

where H denotes the convolution matrix and Δ denotes a diagonal matrix representing v_p. $C_t(t)$ is a matrix consisting of the tissue concentration curves input to the algorithm. This function (Eq. 2.2) is minimized by alternately varying the kinetic parameters and the AIF. A population averaged input function, which has been shown to yield reasonable estimates for kinetic parameters [**?**], is used as the initial guess for the AIF. The initial guesses for pharmacokinetic parameter values are estimated via a nonlinear least squares algorithm using this initial guess for the AIF. The pharmacokinetic parameter values are then held fixed and a new AIF estimate is computed by the same least squares algorithm. This alternating optimization continues until the regression has converged to an AIF. In our implementation the MATLAB lsqcurvefit function was used to perform the nonlinear regressions. Default convergence criteria were used, and parameter values were bounded to prevent nonphysiological negative values.

We use a model parameterization of the following form to represent the AIF [**?**]:

$$C_p(t) = \sum_{i=1..2} A_i \gamma_v(\alpha_i, \tau_i) + A_3 S(\alpha_3, \tau_3, T, \Delta) \tag{2.3}$$

which consists of two normalized gamma variate curves (γ_i) representing the first and second passes of the CA bolus, and a normalized sigmoid function (S) representing

the decaying washout of CA from the ROI. This function is fully described with 11 parameters, and can model a wide range of physiological input functions, similar to that developed by Parker et al. [**?**]. By choosing a flexible analytic form for the AIF, we minimize the impact of AIF measurement noise, which otherwise could be amplified at each step of the minimization process. At each iteration of the alternating minimization with model (AMM) algorithm, the new AIF estimate is constrained to this functional form by nonlinear regression using a least squares approach.

We also changed the implementation of the minimization process from that in [**?**] to include a delay time between the arrival of the CA bolus in the arterial blood and in the tissue of interest. During each iteration, when fitting the tissue curves to the AIF, the AIF was allowed to shift in time to obtain a best fit.

As reported in [**?**], the IQML algorithm can only estimate K^{trans} to within a global scaling constant. To constrain this scale factor, at the end of each iteration the average value of the last five values of the estimated AIF is normalized to the average of the last five time points of the AIF obtained from a nearby region of arterial voxels. At the beginning of the next iteration the estimated AIF is adjusted so that the average concentration of the tail of the estimated AIF matches that of the measured arterial voxels. In practice, it is assumed that following the imaging of the FOV of interest a few images of a nearby artery would be acquired. This acquisition could be optimized for concentration measurements of the equilibrium blood pool concentration. The lower CA concentration several minutes after injection would be less susceptible to nonlinear saturation effects. In addition, moving the imaging FOV to a larger artery would lessen the impact of partial volume effects, allowing for a better estimate for the scaling constant for the estimated AIF. This AIF can then be used with any conventional deconvolution or curve fitting methods to determine kinetic parameters for any pixel in the FOV. The sequence of steps leading to the determination of the AIF is summarized in Figure 2.1.

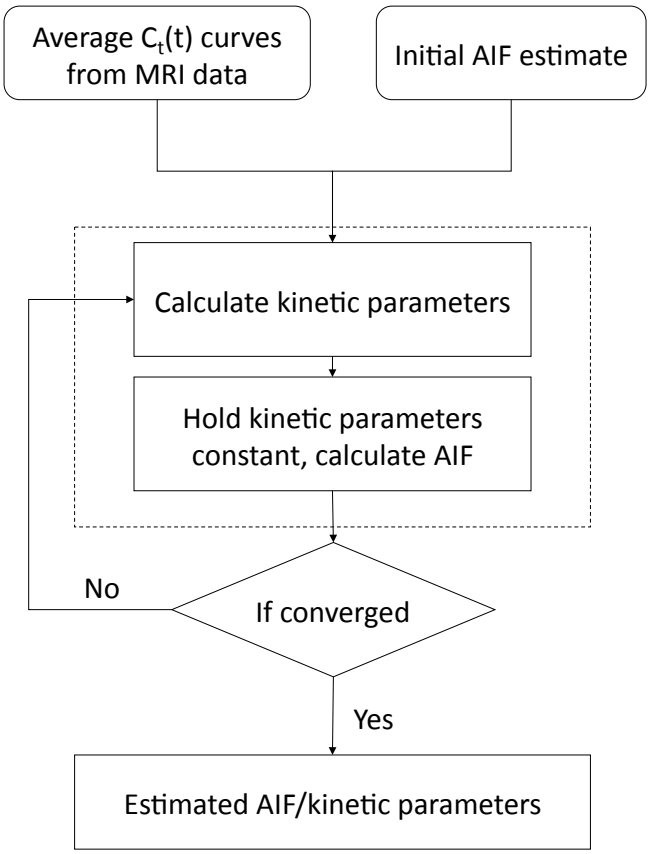

Figure 2.1. Flowchart for the AMM method. This method requires several tissue concentration curves and some estimate for the AIF as input. The algorithm will alternately calculate the kinetic parameters for each input concentration curve and the common input function.

2.2.2 Sensitivity to Initial Estimate of AIF Parameters

The AMM method uses a population averaged input function as a starting guess. To test the sensitivity of the algorithm to this initial guess for the AIF, we generated simulated tissue concentration curves using a model AIF generated using equation 2.3 with the following parameter values: $A_1 = 7.8$, $\alpha_1 = 1.26$, $\tau_1 = 0.00663$, $A_2 = 1.2$, $\alpha_2 = 1.65$, $\tau_2 = 0.00555$, $A_3 = 1.9$, $\alpha_3 = 44$, $\tau_3 = 0.018$, $\Delta = 0.7$, and $T = 15$. Both the AIF and tissue curves were discretized at 4.5 s temporal resolution and truncated after 7.5 min. The resulting AIF is shown in Figure 2.2.

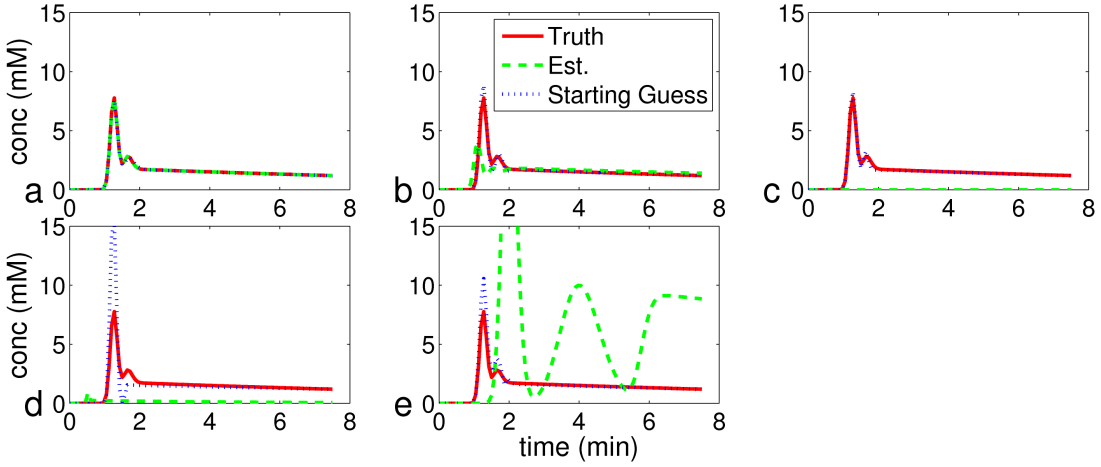

Figure 2.2. Estimated AIFs resulting from variations in initial guess to the AMM method (blue). The initial guess used (green) were truth (a), near truth (b), zero (c), and the lower bounds (d), and upper (e) bounds on the constraints used in the estimation algorithm. For comparison, truth has been plotted on each panel (red). All graphs have the same temporal resolution, shown in red.

Ten sets of four tissue curves were created from the true AIF with pharmacokinetic parameters drawn from a uniform random distribution. K^{trans} was constrained to [0,2.2] $\frac{1}{min}$, v_e to [0.15,1], and v_p to [0,0.2]. Zero mean Gaussian noise with a standard deviation of 0.08 mM, corresponding to an average signal to noise ratio (SNR) of 8 was added to the simulated tissue curves and each set of four curves were input to the AMM method for each of five different initial guesses for the AIF.

The five initial guesses supplied to the AMM algorithm were as follows: the true AIF, a slightly modified version of the true AIF with parameters $A_1 = 4$, $\alpha_1 = 1.1$, $\tau_1 = .009$, $A_2 = 1.5$, $\alpha_2 = 1.5$, $\tau_2 = .01$, $A_3 = 2$, $\alpha_3 = 40$, $\tau_3 = .03$, $\Delta = 0.5$, and $T = 20$; a zero valued vector; and the lower- and upper-bounded AIF from the minimization process, with parameters $A_1 = 1$, $\alpha_1 = 0.5$, $\tau_1 = 0.002$, $A_2 = 0.25$, $\alpha_2 = 0.5$, $\tau_2 = 0.002$, $A_3 = 0.25$, $\alpha_3 = 5$, $\tau_3 = 0.001$, $\Delta = 0.5$, and $T = 5$; and $A_1 = 30$, $\alpha_1 = 2$, $\tau_1 = 0.01$, $A_2 = 10$, $\alpha_2 = 4$, $\tau_2 = 0.03$, $A_3 = 10$, $\alpha_3 = 60$, $\tau_3 = 0.05$, $\Delta = 4$, and $T = 30$, respectively.

The process was repeated for each initial guess with each set of four randomly generated tissue curves. Estimates for the pharmacokinetic parameters for each of the four input curves were calculated. The relative error of these estimates was

computed as a measure of the error introduced by the variation in initial guess.

2.2.3 Noise Sensitivity Simulation

Kinetic parameter estimates from the AMM algorithm were compared to parameter estimates from a measured AIF with a noise simulation based on patient data. A portion of a single slice of patient data with a significant amount of diseased tissue was selected. The measured AIF from this scan was then fit to the model in equation 2.3, and this AIF was used to estimate kinetic parameters for the region. The AIF and estimated parameters were then treated as truth and noise free tissue curves were created according to equation 2.1 with temporal resolution of 4.5 s/frame. Four sets of kinetic parameters were randomly generated within bounds set to match those from the patient data, and zero mean Gaussian noise with standard deviations of 0.02, 0.04, 0.08, and 0.16 mM was added to the tissue curves. For reference, the average standard deviation in the background noise in the original measured data was 0.08 mM, which corresponds to an SNR on the order of 8.

For conventional (nonblind) estimation of the kinetic parameters from the simulated data, noise corresponding to the level added to the tissue curves was added to the simulated AIF, scaled by the square root of 19, which was the number of pixels used to calculate the AIF in the original dataset. The AIF was shifted by a random fraction of the sampling time to simulate jitter. The jittered AIF was then used to calculate the kinetic parameters.

For the blind estimation method, the kinetic parameters were estimated using the AMM algorithm. In addition, the blind estimation algorithm was implemented at each noise level without including any analytic form for the input function. A total of 100 noise realizations were used at each noise level, with four new tissue curves generated randomly at each realization. The conventional AIF was jittered during each realization. The resultant kinetic parameters from the simulated measured AIF, the AMM method, and the alternating minimization without model were then compared with truth, and the relative error was computed.

The noise sensitivity simulation was repeated with a second set of patient data. This set was selected for having the AIF that was the most widely dispersed in time

over all of the patient data used in this work. The simulation methodology was identical to that used with the first patient AIF.

2.2.4 Patient Data

The blind estimation algorithm was applied to DCE-MRI data from 12 patients diagnosed with various soft tissue sarcomas. Data were acquired on a Siemens 1.5T scanner using a fast low angle shot (FLASH) three-dimensional (3D) sequence with 20° flip angle, and TR ranging from 2.81 ms to 3.59 ms and TE ranging from 1.13 ms to 1.44 ms. A total of 20 ml of Omniscan was administered intravenously with a dose of 0.1 mmol/kg to 0.2 mmol/kg of body weight. The temporal resolution of the scans ranged from 3.5 s/frame to 4.9 s/frame. From 12 to 18 slices were obtained from each scan, with 96 to 512 voxels acquired along the frequency axis and 128 to 512 voxels along the phase encode axis. All data were obtained with written consent and was institutional review board (IRB)approved. Measured DCE-MRI images were converted into CA concentration by solving the nonlinear relationship between the FLASH signal and CA concentration, as described in [**?**]. Precontrast T10 values were determined using a variable flip angle method [**?**]. This nonlinear conversion technique minimizes the impact of underestimation of true contrast concentration due to signal saturation at high CA concentrations.

Each dataset contained arterial voxels from which a measured AIF was extracted. The AIF used was selected from the voxels with the highest overall concentration values and earliest uptake times. The AIF selection was done automatically, similar to the method described in [**?**]. This measured AIF functioned as truth in comparison with the blind estimation extracted AIF. Due to the large size of the patient data sets a portion of a single slice through the lesion of interest was selected from each patient for analysis, with the portions averaging 250 X 250 voxels. Each slice was selected so that it also contained arterial voxels, as determined by the AIF measurement technique described above, and the blind estimation algorithm was applied twice. During the second run, any arterial voxels in the selected slice were excluded from use in the blind estimation. The arterial voxels were selected for exclusion based on their shape, specifically the ratio of the height of the first pass of the CA bolus to the

average concentration over the rest of the curve. This was done to test the assumption that AMM may be used in situations where no artery exists within the imaged FOV, or when the clinician may wish to limit the FOV to the region immediately surrounding the area of interest. In both cases, the automatically extracted AIF was used to scale the estimated AIF as described above.

In order to determine the set of curves, here called $C_t(t)$ or tissue concentration curves, to be input into the alternating minimization, the data are clustered into groups of similar curves using an unsupervised k-means algorithm. The number of clusters is determined empirically with the goal that each cluster has a minimum of intracluster variability, here defined as the average of the within cluster sums of point to centroid differences, measured as the vector sum of the Euclidean norms. The tissue concentration curves within each cluster are averaged to obtain a representative curve from every cluster. These cluster averaged curves are then used in the implementation of the blind estimation algorithm.

After CA concentration curves have been obtained from the MRI data they are clustered into groups of similar curves with k-means clustering as described above. The total number of clusters selected is limited by the number of voxels in the dataset under investigation. Smaller datasets yield clusters with fewer tissue concentration curves per cluster. These small clusters produce average curves with lower SNR than would result when opting to use less clusters. With patient data, the algorithm returned nearly identical values for the pharmacokinetic parameters over a range of four to 10 clusters in each dataset. In most instances, eight clusters seemed adequate from empirical testing and eight clusters were used throughout for the patient data.

After an estimated input function has been obtained from the AMM method, kinetic parameter estimates were obtained voxelwise via a linearized least squares approach outlined in [**?**]. This approach was selected for its increased speed with respect to nonlinear approaches.

2.3 Results

2.3.1 Sensitivity to Initial Estimate of AIF Parameters

Mean estimated AIFs from each of the five initial guesses are shown in Figure 2.2. When the initial guess for the AIF matches truth, the algorithm converges rapidly (often in a single iteration) (Figure 2.2a). When the initial guess is close to truth (Figure 2.2b) or uniformly zero (Figure 2.2c), the resulting AIF results in kinetic parameters estimates with a median relative error of 8%. Figure 2.2d represents the lower bound on the 11 AIF parameters in the AMM process. This very poor initial guess for the AIF results in a 300% overestimation of the peak value of the AIF, with a corresponding 65% median relative error in the kinetic parameters. Figure 2.2e represents another intentionally poor initial estimate, the upper bound on the 11 AIF parameters, and results in an AIF yielding 15% median relative error in the kinetic parameters.

2.3.2 Noise Sensitivity Simulation

As stated above, the sensitivity of the algorithm to noise was determined by adding Gaussian noise to a set of tissue curves before applying the blind estimation process. The accuracy of the algorithm was determined by the relative error of the fit kinetic parameters. As shown in Figure 2.3, the average error in K^{trans} and k_{ep} estimates is 5% higher for the AMM method as compared to the more conventional, measured AIF method. The minimization without model results for K^{trans} have the same error as the AMM method at noise levels of 0.04 mM and smaller, but as noise increases, the relative error increases to a maximum of 36%, with the AMM maximum at 22%. The estimates for k_{ep} are not as good when the AIF model was not used, with an average of 13% higher relative error as compared to AMM. v_p measurements were highly sensitive to small variations in the estimated input function. In addition, v_p measurements tend to be on the order of 0.10, and thus small changes in the estimates yield high percentage errors. All of the analysis methods had some error at a zero noise level. This error is due to the coarse temporal resolution used in these simulations. When the temporal resolution was increased to 0.5 s per time sample, all the estimation techniques returned zero error when no noise was added to the

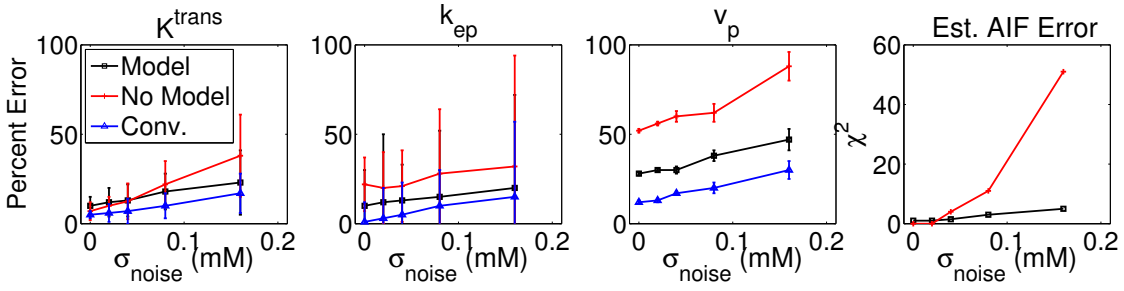

Figure 2.3. The relative error in estimated kinetic parameters after noise has been added to simulated tissue concentration curves. The error in the kinetic parameters was less when the functional model for the AIF was included in the alternating minimization (black), as compared to when no restrictions were placed on the input function (red), and is 10% higher than the error from measurements using a conventionally acquired AIF (blue). The χ^2 fits of the estimated input functions are also shown.

simulated curves. Representative results from a single noise realization at a noise level of 0.08 mM are shown in Figure 2.4 for both of the test AIFs.

2.3.3 Patient Data

Figure 2.5 shows the tissue concentration curves from one representative cluster along with the average cluster value used in the AMM process. Averaging the curves in each cluster served to reduce the noise in the data and provided a representative value for the curves in the cluster.

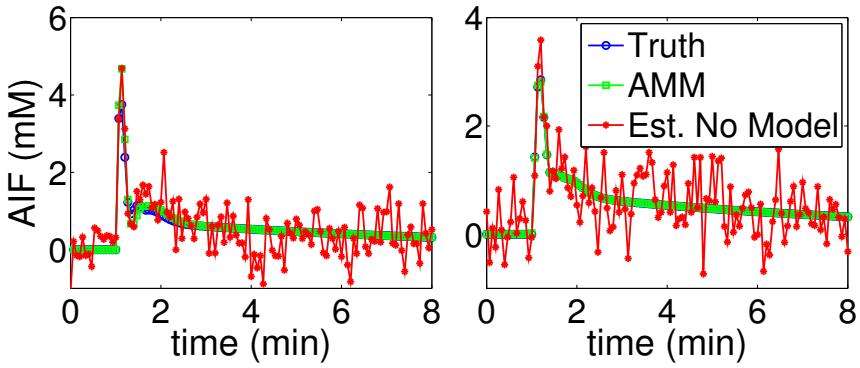

Figure 2.4. AIFs used in noise sensitivity simulation (blue). Representative estimated AIFs from the AMM method when the model was included (green) and not included (red) are also shown.

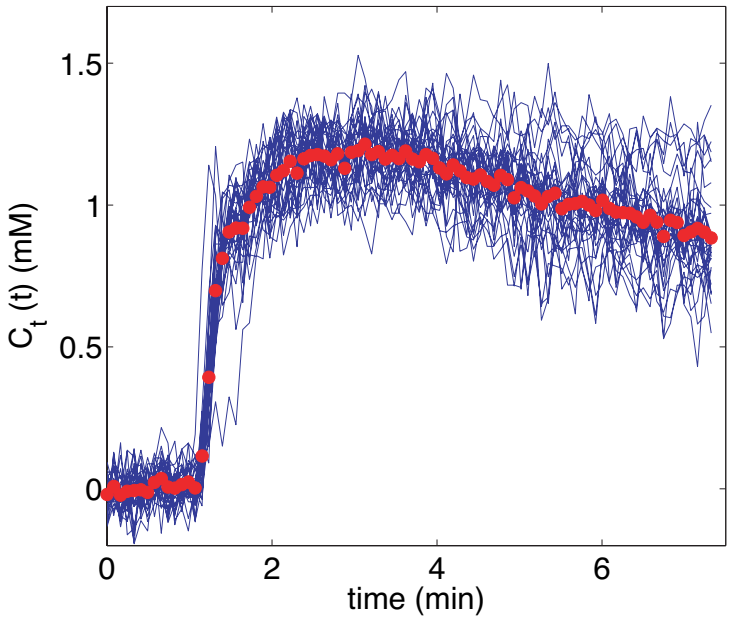

Figure 2.5. Representative tissue concentration curve cluster from a sarcoma patient. The blue curves represent single voxel activity from the tumor rim. The bold red circles indicate the average value of all curves in this cluster, and were used as an input to the AMM algorithm.

Figure 2.6 shows results from the AMM process for a patient. The fitted curves closely match the measured data during the initial arrival of CA to the tissue. Overall curve fitting has similar χ^2 values to that done with arterially measured AIFs.

Representative maps of kinetic parameters from the same patient are shown in Figures 2.7 and 2.8. Kinetic parameters were obtained by the method described [**?**], using the measured AIF from the DCE-MRI data (Figures 2.7 and 2.8, first row), and those computed by the AMM method (Figures 2.7 and 2.8, second row). The AIFs from the AMM method in Figure 2.7 were estimated when arterial voxels were included in clustering. The parameters obtained from the estimated AIF are lower than those from the measured AIF due to the increased peak height in the estimated AIF over the measured AIF. In Figure 2.8, arterial voxels were not included in the estimation process. The K^{trans} and k_{ep} values obtained from the estimated AIF are lower than those from the measured AIF, though the v_p values are higher. Figure 2.9 shows the measured AIF from this patient's data. The measured AIF for this

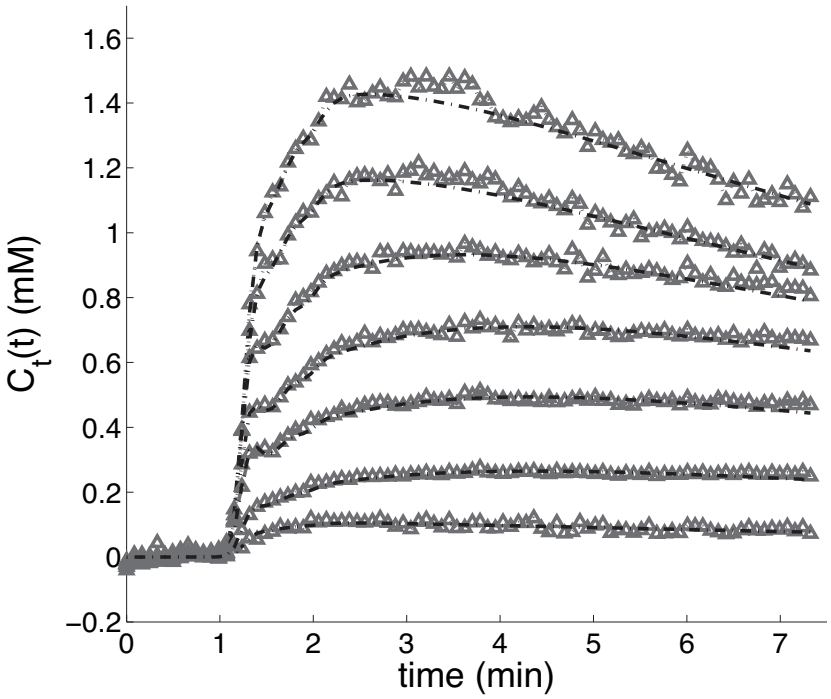

Figure 2.6. Curve fitting results from the AMM algorithm with eight clusters used as the input. The gray points represent the average valued curves from each cluster. The dashed line functions were constructed from the estimated kinetic parameters and AIF from the AMM algorithm, according to the two compartment model. The eighth cluster contained only background noise and has been deleted.

patient was extracted from a mix of arterial and venous voxels, affecting the quality of measurement. As the accuracy of the measured AIF is suspect for the patient in Figures 2.7 through 2.9, the agreement of the kinetic parameters in Figures 2.7 and 2.8 and plots are not representative, as can be seen by noting the aggregate differences shown in Figure 2.11 are typically smaller. In addition the tissue AIFs resulting from the AMM method with and without the inclusion of arterial voxels are overlaid for easy comparison. For each of the 12 datasets, three ROIs were drawn and used to calculate average kinetic parameters. Two ROIs were selected from a region of diseased tissue, the other from a region of healthy tissue (Figure 2.10). The average values of the kinetic parameters for these regions are summarized in Figure 2.11. The average K^{trans} values resulting from the measured AIF are 13% higher than those from the AMM derived AIFs with arterial voxels and 16% higher than those from

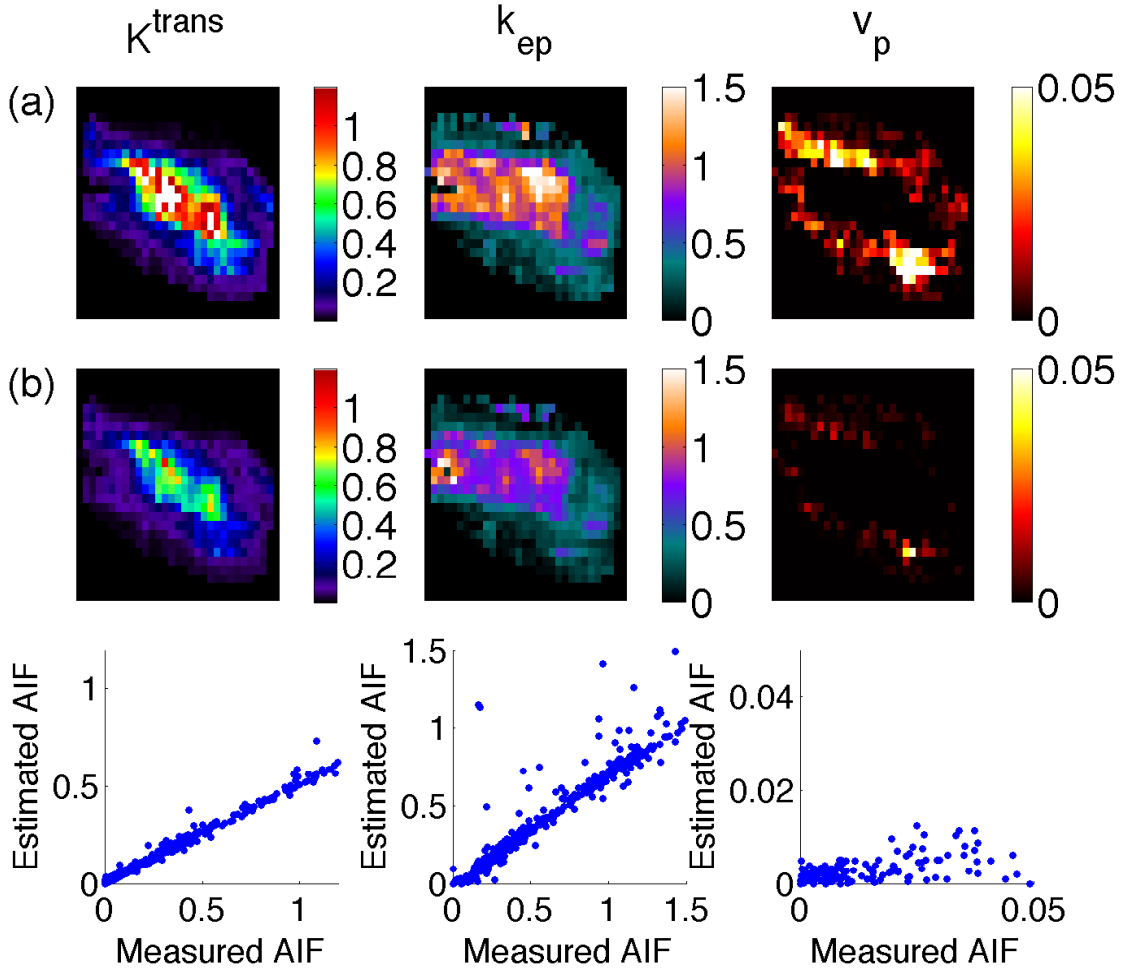

Figure 2.7. Parameter mapping results. The first row (a) used the measured AIF. The second row (b) was derived from the estimated AIF using arterial voxels. The third row shows scatter plots of the parameters displayed in row (a) (x-axis) and row (b) (y-axis). The patient was scanned near the proximal humerus, with the AIF measured in the brachial artery. The region shown is from a primitive neuroectodermal tumor.

AMM when arterial voxels were excluded. The average k_{ep} values obtained from the measured AIFs were 7.5% higher than those from the AMM method with or without arterial voxels. The measured AIF and arterial voxel AMM average values for v_p differ by< 0.007 while those resulting from AMM without arterial voxels are approximately 0.1 higher. A two tailed dependent Students t-test showed that the differences in parameters were not significant ($P > 0.5$) with the exception of the differences in v_p estimated with the measured AIF and the estimated AIF when arterial voxels

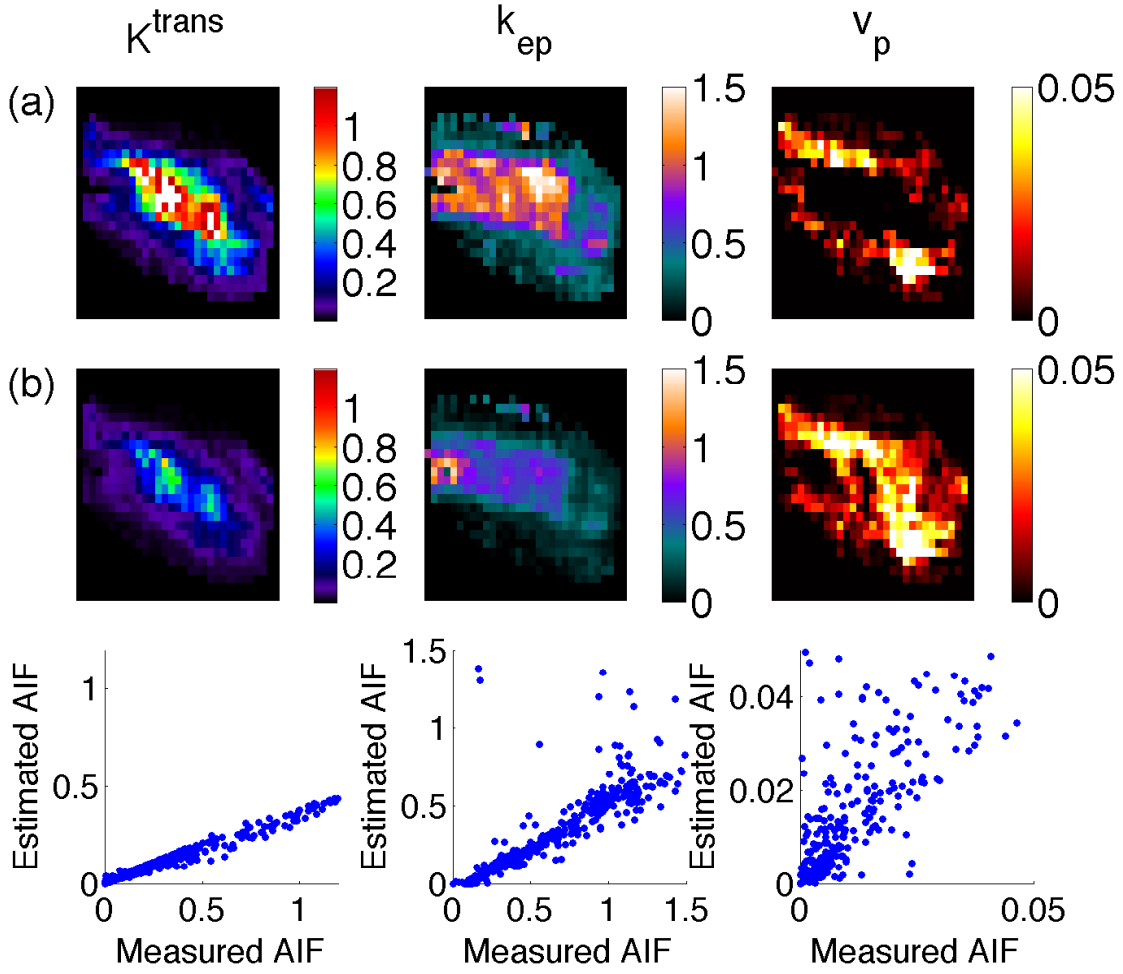

Figure 2.8. Parameter mapping results. The first row (a) used the measured AIF. The second row (b) was derived from the AIF estimated when arterial voxels were excluded. The third row shows scatter plots of the parameters displayed in row (a) (x-axis) and row (b) (y-axis). These maps correspond to the same region as in Figure 2.7

were excluded (P = 0.0005). The differences in kinetic parameters result from the different shape in the resulting AIFs from the AMM method when arterial voxels are included and excluded in the estimation. Figure 2.12 shows the mean and standard deviation of the AIFs from the patient data, one of which included arterial voxels, and one resulting from the exclusion of that data. The distinctly different heights and widths of the estimated AIF during the first pass of the bolus suggest that the inclusion of arterial voxels impacts the estimated AIF.

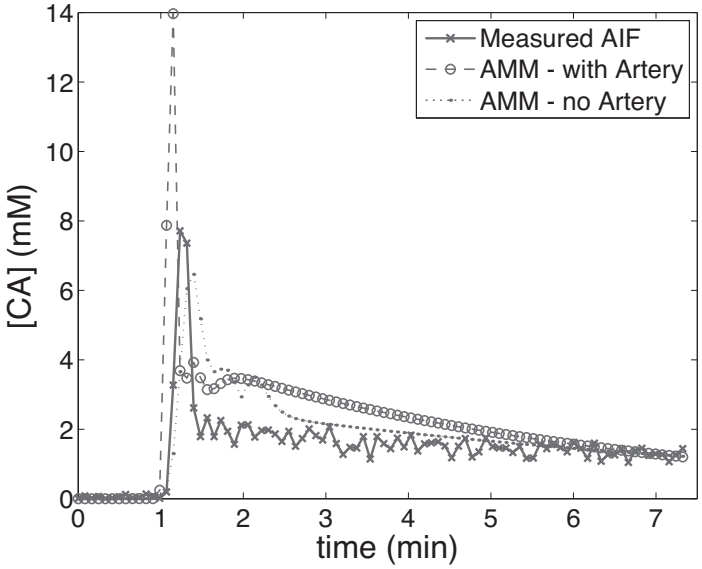

Figure 2.9. AIFs from the patient data seen in Figures 2.7 and 2.8. The measured AIF was obtained through an automated process similar to that described [**?**], and the tissue AIFs are the result of the AMM algorithm when arterial voxels were included and excluded.

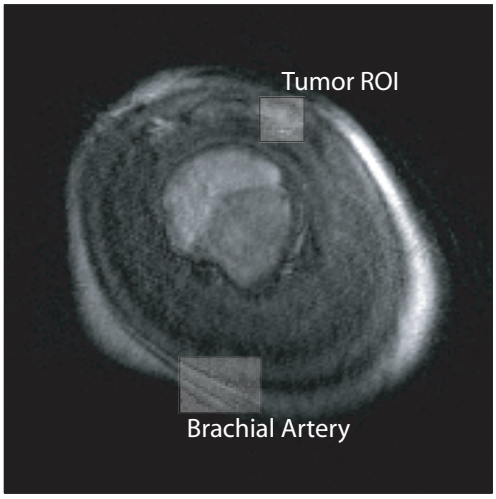

Figure 2.10. A postcontrast slice frame of this patients DCE-MRI data is included for reference. The brachial artery, from which the measured AIF was obtained, and the tumor ROI are highlighted.

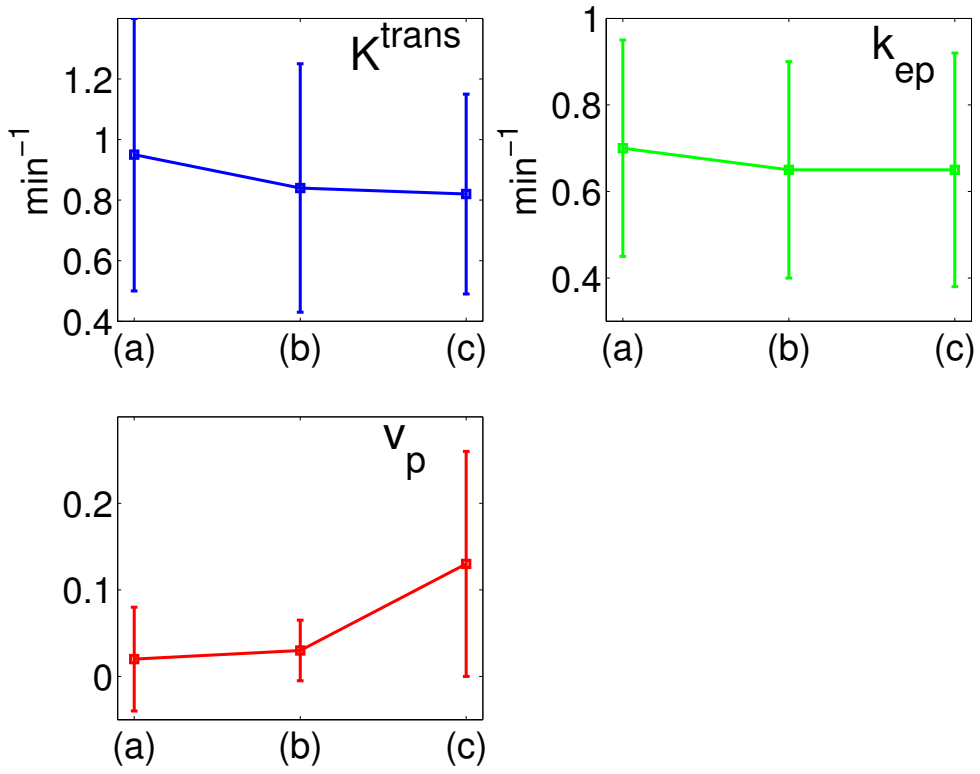

Figure 2.11. Relative mean changes for each of the pharmacokinetic parameters and standard deviation of each measurement. The parameters were measured from 12 patients, with two ROIs selected from each patient. Each chart shows the parameter value when derived from the measured AIF (a), the estimated AIF when arterial voxels are included (b), and the estimated AIF when arterial voxels are excluded (c).

2.4 Discussion

Here we have presented a method for estimating pharmacokinetic parameters from DCE-MRI data without explicitly measuring the AIF. Reference region methods for determining kinetic parameters without a measured AIF have been proposed [?, ?, ?, ?]. However, these methods require the use of one or more reference regions for which assumed values for the kinetic parameters for these reference regions must be provided. While the reference region approach appears fairly robust in dealing with low SNR data and has been shown to give results similar to those derived from a known AIF, the assumptions inherent in this class of methods may lead to unnecessary bias in the resulting kinetic parameters. For instance, though literature values for kinetic parameters in reference regions may be generally accurate, they do

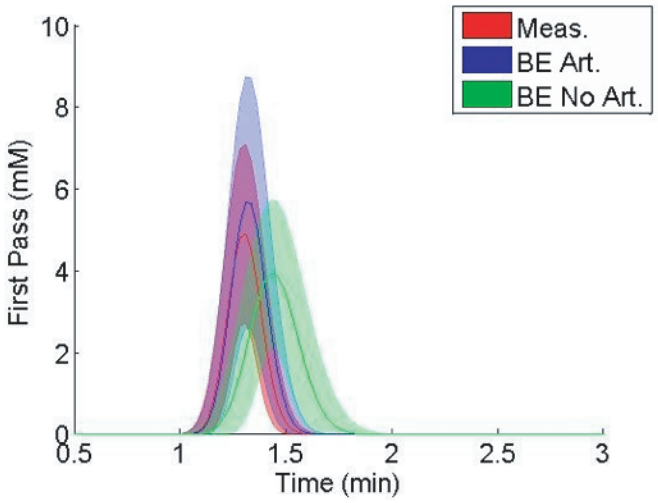

Figure 2.12. Average performance of the AMM algorithm for 12 patients. The curves represent the mean (center) and standard deviation of the first pass bolus of the AIF derived from measured voxels (red), or from the AMM method when arterial voxels are included (blue) and excluded (green). The first gamma variate curve from the AMM model was used to describe the first pass.

not allow for interpatient individuality and thus introduce some bias into the results.

A method similar to the one described here has been proposed by Yang et al. [**?**, **?**] that makes use of multiple tissue concentration regions used jointly to identify kinetic parameters and an AIF simultaneously. This method imposes a local polynomial smoothing to ensure a smooth form for the AIF curve. In addition, one region used in this method is assumed to be skeletal muscle in which the v_p term is forced to be close to or equal to zero. As well, v_e is set to 0.12 in the skeletal muscle region in their model. This is done to provide a reference for the general scale factor needed to quantify estimated parameters. This method performed well on real data when one concentration region contained a high percentage of pixels with arterial blood, but was only demonstrated on a single patient [**?**].

The AMM method presented here uses tissue concentration curves from a portion of the image and blindly estimates the input function through an iterative algorithm. The basic assumptions in this method are common to the extended Tofts-Kety two compartment model: tissues may be represented as separate compartments in and out of which CA is free to diffuse. Additionally, the CA is assumed to be well mixed

within the blood pool in the fast exchange limit. The AMM method is unique in assuming a novel functional form for the input function as defined in equation 2.3. Analytical forms for the input function in dynamic imaging have been proposed with Gaussian [**?**] and exponential or multiexponential [**?**, **?**] curves. The particular form chosen here was selected for its flexibility and quality of fit across multiple datasets. For blind estimation, constraining the input function to a particular functional form ensures smoothness and increases the efficiency of the algorithm by limiting the number of unknown variables. When the input function was allowed to vary without any constraints in the algorithm, the resulting AIF was significantly noisier than the tissue curves. The simulations also showed that kinetic parameter measurements are more accurate at higher levels of noise when the input function model is included. This suggests that the model constraint helps prevent the iterative estimation from amplifying noise. Without the AIF model, the characteristic dispersion in the first pass of the bolus for cases in which arteries were excluded from the FOV was still present, signifying that this dispersion is not a consequence of the use of the AIF model.

One possible source for error in the AMM algorithm is the selection of initial estimates. By restricting the AIF to the functional form of equation 2.3, we can standardize the form for guesses in the initial AIF. Additionally, this functional form avoids the characteristic underestimation found in other models for the AIF [**?**]. The AMM algorithm was shown here to be robust to variation in the initial AIF if the initial AIF was somewhat similar to the true AIF or was all zeros. Artificial initial estimates that would be difficult to rationalize in practice gave poor results. The model parameters for the AIF were bounded to a range broad enough to model the AIFs from each of the patients tested in this study. These bounds provided limits for the least squares algorithm.

As shown in Figure 2.12, the algorithm presented here estimates different peak values and transit times of the CA bolus in the AIF, depending on whether arterial voxels are included as inputs to the AMM process. Calamante et al. [**?**] and Calamente [**?**] have investigated the effects of local AIFs in DSC-MRI perfusion studies. Typical DCE-MRI studies involve measuring the input function $C_p(t)$ in some artery

convenient to the ROI. However, CA molecules perfuse tissue through exchange across the capillary bed vascular endothelium, which lies significantly downstream from the large arteries used for AIF measurement. Early studies assumed minimal differences between the AIF and CA concentration in the capillary bed. However, studies such as those by Calamante et al. [**?**] and Calamante [**?**] have found evidence suggesting the true local input function may be appreciably dispersed in time, similar to the results we show here. Also, Schmitt et al. [**?**] have examined the possible effects of dispersion and delay in simulated input functions in DCE myocardial blood flow measurements. They report systematic underestimations of up to 50% in blood flow measurements due to input function dispersion. Our results, as seen in Figure 2.12, support the idea that local input functions may be significantly delayed and dispersed as compared to measured AIFs. A limitation of this study is that measured AIFs may not always provide a suitable reference standard. Although the method in [**?**] was used, there may be inclusion of venous signal in some cases as well as partial volume effects that will tend to reduce the peak of measured AIF. It is not surprising then that the AMM method with arteries in the field of view tends to estimate an AIF with a higher peak. In particular, the dispersed form of the AIF generally results in superior tissue curve fits compared to the nondispersed form. Further investigation into the nature of AIF dispersion in microvasculature may help clarify the nature of CA delivery.

2.5 Conclusions

We set out to develop an accurate method for blindly estimating CA input functions for use in DCE-MRI studies. The motivation for this research was to allow for increased flexibility in imaging parameters by removing any requirement for arterial voxels in the imaging FOV. In order to reduce noise effects and optimize computational time, we assumed a parameterized model for the input function, using 11 parameters. This model based blind estimation method outperformed our previous method that did not include a model of the AIF, with 10% to 20% lower relative error. The blind estimation was shown to be robust to guesses for the input function, and was relatively robust to noise. Results from human studies in regions without

arterial voxels returned input functions that demonstrated significant dispersion as compared to the measured AIFs from these data sets. These results support the idea of unique local input functions in the regions of interest. Further work is required to investigate the spatial variance of CA input to tissues in DCE-MRI.

CHAPTER 3

LOCAL ARTERIAL INPUT FUNCTIONS

Portions of this chapter originally appeared in "Towards Local Arterial Input Functions in Dynamic Contrast-Enhanced MRI" J. Mag Res Im. Volume 32 Issue 4 Pages 924-934. Reprinted with permission

3.1 Introduction

This chapter builds upon the alternating minimization with model (AMM) method for blind AIF estimation. In the previous chapter it was observed that, applied to clinically acquired data, the AMM algorithm produced different AIF estimates depending on the type of tissue concentration curves used as input. When arterial voxels were included, the estimated AIF closely matched the directly measured AIF. In contrast, when the region of interest was localized to contain only enhancing tissue voxels, the estimated AIF was both delayed and dispersed with respect to the directly measured AIF. Previous research in dynamic susceptibility contrast in brain imaging by Calamante et al. [**?**, **?**] supports the idea that local input functions exhibit delay and dispersion with respect to AIFs measured in central arteries due to transit effects as the contrast bolus traverses the vasculature. Dispersion in the arterial input function has been shown with computer simulations to have a significant effect on the resulting parameter estimates [**?**].

Previous work with the AMM method focused on the estimation of a single tumor wide AIF. Additionally, the impact of the number and heterogeneity of the selected tissue curves on the quality of blind AIF estimates has not previously been investigated. In this chapter we use computer simulations to develop a new confidence measurement for use in conjunction with AMM estimations. The new metric relates the number and heterogeneity of the input tissue curves to the quality of the resulting

blind AIF estimate. This confidence metric can then be used in the processing of in vivo DCE-MRI data sets to define subsets of voxels that contain a sufficient number of heterogeneous tissue curves to estimate an input function, locally (i.e., a region size 10X10X10 voxels), with known accuracy. These local arterial input functions are then used to estimate pharmacokinetic parameters voxelwise within the subset from which they were created.

Here we present preliminary results comparing the kinetic parameters and goodness of fits obtained from local AIFs to those from blind AIFs estimated globally across the field of view and those from arterially measured AIFs.

3.2 Methods

3.2.1 Confidence Measurements

Both empirical observations, and previous theoretical studies [**?**] suggest that there are two key factors determining convergence of the AMM algorithm: 1) the concentration signal to noise ratio (SNR) of the tissue concentration curves $[C_t(t)]$ used to estimate the AIF, and 2) the heterogeneity, or diversity, of the kinetic parameters among the curve set. Here we define concentration signal to noise as the ratio of the peak concentration value of a tissue curve to the standard deviation of the baseline concentration measurements. We quantify diversity by assessing the normalized spread of k_{ep}, and v_p in parameter space. K^{trans} is essentially a scale factor in the tissue curve model which does not add any information regarding the shape of the underlying AIF and thus is not included in the measure of diversity (though since it partly determines concentration SNR, K^{trans} does affect the confidence calculation).

A series of simulations were undertaken to assess the impact of tissue curve SNR and diversity on AMM AIF estimation. The simulation proceeded as follows:

1. Two simulated AIFs (one to serve as truth, and the second to initialize the AMM estimation) were created using the model form [**?**]:

$$C_p(t) = \sum_{i=1..3} A_i \gamma_v(\alpha_i, \tau_i, \Delta_i) + A_4 S(\alpha_4, \tau_4, T, \Delta_4) \tag{3.1}$$

where γ_v refers to a gamma variate function and S refers to a sigmoid function. In this model A_i are scaling constants, Δ_i are related to the injection time, and

α_i, τ_i and T are related to the shape and concentration of the bolus. In these simulations the true AIF was selected to be different from the population AIF so that the initial AIF guess in the AMM algorithm, which was set as the population average AIF, would not be the same as truth. The true AIF had parameters: $A_1 = 4.83$, $\alpha_{1-4} = 4.99$, $\tau_1 = 0.0564$, $\Delta_1 = 1.0$, $A_2 = 0.24$, $\tau_{2-4} = 0.0731$, $\Delta_2 = 1.3$, $A_3 = 0.11$, $\Delta_{3-4} = 1.6$, $A_4 = 0.21$, and $T = 14.42$. and was sampled with 4s temporal resolution. This true AIF is slightly dispersed and delayed with respect to the population-average AIF given by Parker. The AIF model in equation 3.1 was fit to the population average AIF reported by Parker [**?**] with parameters: $A_1 = 6$, $\alpha_{1-4} = 2.92$, $\tau_1 = 0.0633$, $\Delta_1 = 1.0$, $A_2 = 0.27$, $\tau_{2-4} = 0.0953$, $\Delta_2 = 1.3$, $A_3 = 0.12$, $\Delta_{3-4} = 1.9$, $A_4 = 0.21$, and $T = 14.712$. The true AIF used in these simulations can be seen in Figure 3.1 along with the population average AIF.

2. 6000 sets of eight curves each were created from kinetic parameters randomly selected from uniform distributions of varying size, selected to cover the full range of diversities seen in previously measured patient data.

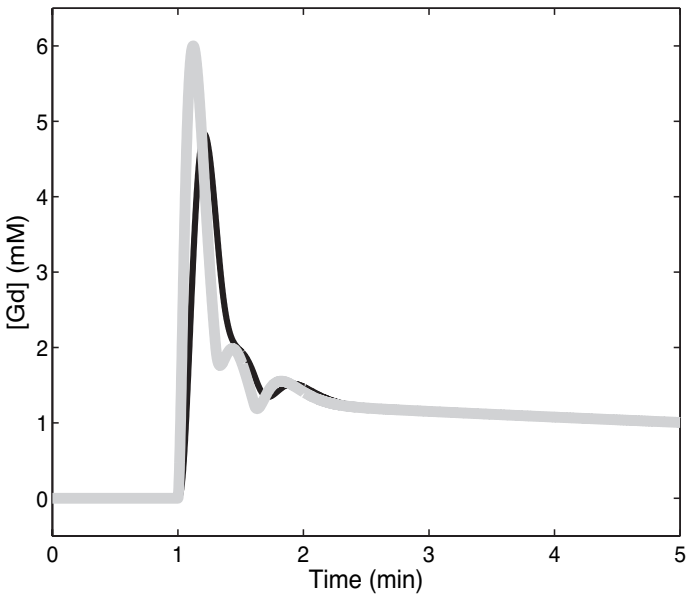

Figure 3.1. AIFs used for confidence simulations. The true AIF (thin black line) is slightly dispersed with respect to the population average (thick gray line) AIF.

3. Zero mean, Gaussian noise with standard deviation of 0.02mM, which corresponds to the average noise level observed in lesions in our patient data, was added to the first 2000 sets of eight curves. Noise with standard deviations of 0.03mM and 0.04mM were added to the second 2000 and third 2000 sets of eight curves, respectively. Each set of eight simulated, noisy tissue curves was then used as input to the AMM algorithm. The initial guess for the algorithm in each case was the population average AIF.

4. Following the estimation of the AIF and kinetic parameters for each realization, the error in the estimated input function was determined. This error was not calculated by direct comparison to the true AIF, but rather by the impact of AIF error on the estimation of kinetic parameters. This error metric was chosen to reflect the importance of the downstream parameters, as well as the indirect relationship between AIF shape and the resulting parameter values. To assess the impact of the estimated AIF shape on kinetic parameter estimates, 1000 tissue curves were generated from randomly selected kinetic parameters and the true AIF. For each of these tissue curves, kinetic parameters were calculated using a linearized form of the extended Kety model [**?**] with the estimated AIF. The median value of the percent error for each of the 1000 kinetic parameters (K^{trans}, k_{ep}, v_p) was used as the overall error for the AIF estimate.

5. For each simulation of eight curves, the diversity of the kinetic parameters in a single noise realization was measured by first normalizing the k_{ep} and v_p values for each of the curves in the set. These normalized values were treated as points in two dimensional parameter space and used as input in MATLABs (The Mathworks Inc, R2007b) `convhulln` routine to create a convex polygon containing all eight points. The area of this polygon was used as the measure for diversity for each simulation. Figure 3.2 demonstrates this calculation for one sample set of eight parameters. This diversity metric was chosen based on the observation that the quality of the AMM derived AIF was dependent on the range of kinetic parameters of the input tissue curves [**?**]. As well, the addition of curves that did not add to the total spread in the parameters did not alter

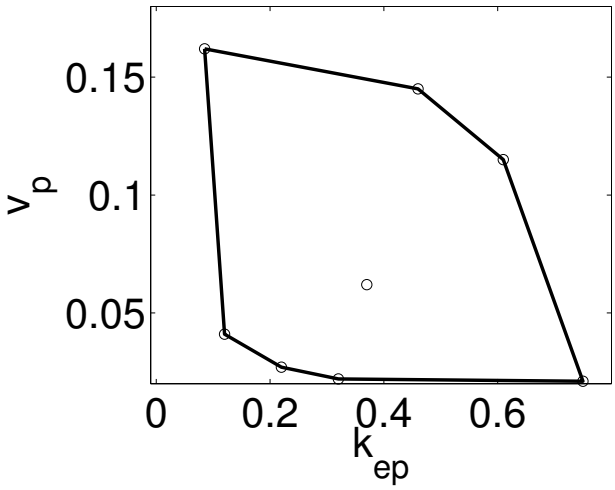

Figure 3.2. A representation of the diversity calculation in two dimensions. Seven of the eight parameter points were used in the convex hull in this example. The point within the hull does not contribute to the diversity measure.

the estimation quality, as defined by the resultant error in kinetic parameters. In the simulations described above, on average 63% of the input tissue curves or clusters contributed to the total diversity, with the remaining 37% being completely contained within the convex polygon created by the other curves.

6. The mean concentration SNR of each set of tissue curves was calculated by first finding the maximum concentration value for each of the eight tissue curves in the set. The average value of these eight maxima was divided by the noise level to create a mean peak concentration SNR measure for each set of curves.

3.2.2 Clinical Data

Local AIF estimates were obtained from 11 patient data sets. Eight of these patients had sarcomas in their arm or leg, while the other three had brain tumors. All data was acquired on a Siemens 1.5T scanner with a FLASH 3D sequence (mean TR/TE=3.16/1.25) and a 20° flip angle. Twenty mL of Omniscan were administered intravenously at a rate of 4mL/s corresponding to a dose of 0.1-0.2 mmol/kg of body weight. The contrast was followed by a 20 mL saline flush at 2 mL/s. The temporal resolution of the scans was approximately 4 seconds/frame. Written consent was obtained from all patients as part of ongoing DCE-MRI studies and IRB approval

was obtained. Prior to contrast injection, T1 values were determined using a variable flip angle method as outlined in [**?**]. Measured DCE-MRI images were converted into CA concentration by solving the non linear relationship between the FLASH signal and CA concentration [**?**]. This method minimizes the impact of concentration measurement error due to signal saturation.

After the patient data were converted to concentration measurements, five adjacent slices of image data containing the tumor were identified. A rectangular region of interest consisting of the tumor and surrounding tissue was selected. A region growing method was developed to select local subsets of voxels for the AMM algorithm. The region growing method used a three-dimensional, concentric search pattern to add new curves to the subset voxelwise, beginning with an arbitrary seed point. As each new voxel was added to the subset, the curves were clustered using an unsupervised k-means algorithm into a set of eight characteristic tissue curves. The SNR and diversity of these characteristic curves were calculated and compared to a user defined threshold. A threshold of 4.7 for combined normalized diversity/SNR, corresponding to an estimated standard deviation of 0.05 in K^{trans} error, was selected, and the region was allowed to grow until the combined peak SNR and diversity reached this threshold or 1000 curves were added to the subset. Seed points were selected from the middle slice of the five slices, and were evenly spaced five voxels apart across the selected region. The characteristic curves from each local region grown subset were input to the AMM algorithm, which estimated a parameterized AIF for each set. AIF estimates were color coded according to the natural logarithm of the estimated error to better show differences in error. These AIFs were then overlaid on the middle slice of MRI data for two representative sample datasets, and kinetic parameters were calculated locally.

The kinetic parameters were determined for every voxel in the selected region by fitting the extended Kety model to the data using the nearest neighbor locally estimated AIF. For comparison, a single global AIF was estimated using the tissue curves from the entire selected tumor. The tissue curves from this whole region were clustered into eight characteristic curves and input to the AMM algorithm, similar to the estimated AIFs from Chapter 2 when no arterial voxels were included. Kinetic

parameters were calculated voxelwise using this globally estimated AIF. In addition, each of the datasets studied here contained large arteries outside the tumor region. A measured AIF was automatically extracted from the top 10% enhancing voxels which had peak values within 30 seconds of the bolus injection time [**?**]. Kinetic parameters were also calculated voxelwise using this measured AIF. Difference maps for each of the kinetic parameters were created by comparing these kinetic parameters to those created from the globally and locally estimated AIFs.

Comparison between the AIFs and associated kinetic parameters was done on a voxelwise basis. Voxels for which the fitting algorithm converged to nonphysical values were excluded from the comparison automatically. For the purposes of this comparison, significance masks were created by restricting K^{trans} to the range [0 5.0] $\frac{1}{min}$, v_e was restricted to the range [0.1 1.0] and v_p to the range [0 1.0] [**?**]. Nonphysical parameter values arise in voxels dominated by noise. Restricting the values to a physiological range, like that reported in [**?**], excludes these voxels. Akaikes information criterion (AIC) was used to determine the goodness of fit for each of the AIF estimation models (i.e., measured, globally estimated, and locally estimated). This criterion takes into account the closeness of the model to the data, as well as the number of parameters used to generate the model. AIC values were computed voxelwise, and the median value over the tumor was calculated for each subject. Kinetic parameters were collected from all of the 11 patients in this study and Pearsons correlation coefficient and the line of best fit were calculated for each of the possible parameter comparisons (i.e., measured-global, measured-local, global-local). Students paired t-test was used to determine if the samples were significantly different at the 5% confidence level. Bonferronis correction was used to adjust for multiple comparisons.

3.3 Results

3.3.1 Confidence Measurements

Figures 3.3 and 3.4 depict the quality of the AIF estimation as a function of both SNR and tissue curve diversity. Figure 3.3(a) shows the relationship of the spread in the percent error of kinetic parameter estimates and the diversity present in the

tissue curve set. Each curve in the figure represents a group of realizations within a specific range of SNR. Two trends are apparent in this graph. The first trend is that as diversity increases within a set, the expected σ_{error} in estimation decreases. As the diversity increases from near zero to values around 20% of the maximum for the simulations, the σ_{error} decreases by 75%. As the diversity continues to increase, the rate of decrease in σ_{error} is approximately linear, with a rate of -.01 σ_{error} for every 20% increase in diversity. Secondly, for a given level of diversity, an increase in SNR will lower the expected σ_{error}. This trend is more readily apparent in Figure 3.3(b), which uses the same data seen in Figure 3.3(a). Here each realization is sorted into groups of similar diversity, and the expected spread in σ_{error} is plotted as a function of increasing SNR. As expected, at a constant diversity level, curve sets with higher SNR will result in better estimations on average. Also, at a given SNR level, an increase in diversity will result in a general decrease in σ_{error}, though the improvement rate decreases as diversity increases. For each curve of constant diversity, as the SNR increases by 25%, the expected σ_{error} decreases by 0.025.

Both Figures 3.3(a) and (b) display expected σ_{error} only for K^{trans}. k_{ep} σ_{error}

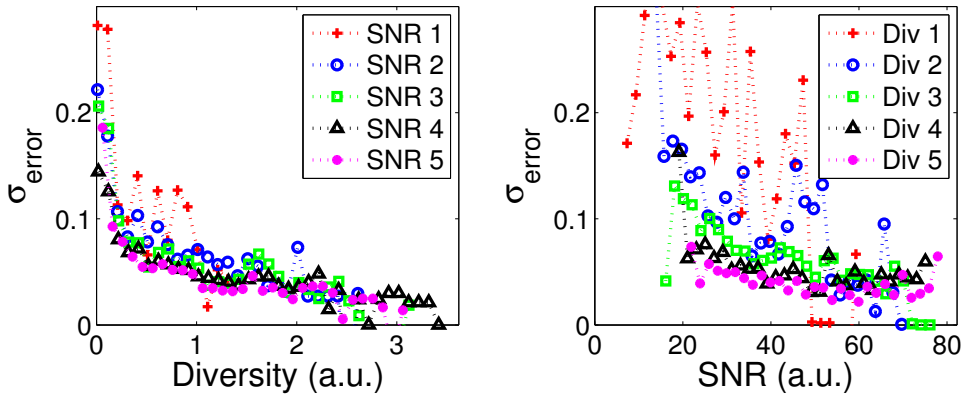

Figure 3.3. The standard deviation of errors for the confidence simulations with respect to diversity (a) and SNR (b). In (a), as the diversity of the tissue curve sets in each group of realizations (sorted by increasing SNR 1-5) increases, the expected σ_{error} decreases for a given SNR level. In (b) the converse is true, at a given level of diversity (sorted by increase diversity 1-5), increasing SNR results in a lower spread in estimation σ_{error}. Only K^{trans} σ_{error} is reported here. k_{ep} errors tend follow those of K^{trans}, while v_p tends to be less affected by SNR and diversity.

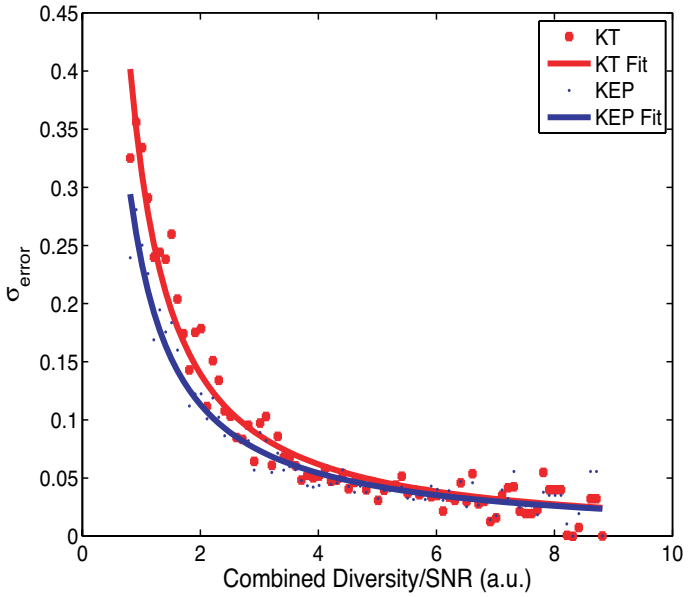

Figure 3.4. The standard deviation of the errors in the confidence simulations plotted with respect to a combined SNR/diversity metric. Both SNR and diversity were normalized to the range [0 5] and the sum of these two metrics was used as the overall quality of fit metric. Both K^{trans} (red +) and k_{ep} (blue diamonds) decreased as a power function of the quality metric. The σ_{error} shown here was error calculated from percent error in kinetic parameter measurements.

tends to follow K^{trans} σ_{error} closely, and is not shown for simplicity's sake. The spread in σ_{error} of the v_p estimates tends to be larger than that for the other kinetic parameters, and remains constant regardless of SNR or diversity. v_p measurements are sensitive to the temporal sampling rate. If the temporal sampling of the data is slower than the Nyquist rate for the associated AIF, the model will not be able to return accurate v_p estimates [**?**].

The overall effects of SNR and diversity are shown in Figure 3.4. Both SNR and diversity were normalized to have the same range, and the sum of the two measures was used as an overall quality metric. Both K^{trans} and k_{ep} σ_{error} are shown in Figure 3.4 to illustrate the close correlation between the two parameters. A power function of the form $y = Ax^b$ was fit to both of the σ_{error} curves with parameters $A = 0.32$, $b = -1.20$ for K^{trans} and $A = 0.24$, $b = -1.10$ for k_{ep}. A power function was chosen as it provided the best fit to the measured results. The parameters A and b do not have a direct physical interpretation, but rather provide an estimate for the

rate at which the estimated quality is expected to improve given an increase in SNR and diversity. At a combined normalized diversity/SNR above 4.7 a.u. the AMM algorithm returns results with a standard deviation of error of less than 0.05.

3.3.2 Clinical Data

Figure 3.5 shows the results of local AIF calculation from a sample data set. This patient was scanned near the proximal humerus, and the AIF was measured in the brachial artery. The region shown is from a primitive neuroectodermal tumor. The MR data in this figure were converted to contrast concentration as described above. All of the region grown subsets within this image had approximately the same level of noise (0.02 mM) with a range of (0.011 to 0.031 mM), although the voxel subset sizes ranged from 10-139 curves. Though the region growing algorithm attempts to find subsets with a given level of SNR and diversity, in some cases the upper bound on the subset size, set here to 1000 curves, was reached before the curves within the subset reached the SNR/diversity threshold. The region within the center of the lesion contained tissue curves with the highest diversity, as signified by the red AIF curves. Regions around the rim of the tumor had less diversity, as shown by the darker red AIF curves. Outside the lesion, the tissue was fairly homogenous, resulting in poor diversity. In addition, the area outside the tumor consisted mainly of skeletal muscle, which was poorly enhancing as compared to the tumor and thus has low concentration SNR. Typical subset sizes in this outer region ranged from 300-1000 curves. The subsets in the center of the lesion resulted in estimated input functions with significant dispersion with respect to the measured AIF.

Similar results from a patient with a brain tumor are shown in Figure 3.6. This patient had a glioma and the AIF was measured in the middle cerebral artery. As with the previous data, the noise level across this image was fairly uniform, with a range of 0.007 to 0.016 mM. The region of highest diversity in this figure came from the subset containing voxels with highly enhancing arterial signal. In this patient, 32 of the 77 subsets contained 1000 curves, while the size of the remaining subsets ranged from 11-1000 curves. The AIF dispersion seen in the previous figure was also present in the tumor center here, though to less degree. Subsets on the side contralateral

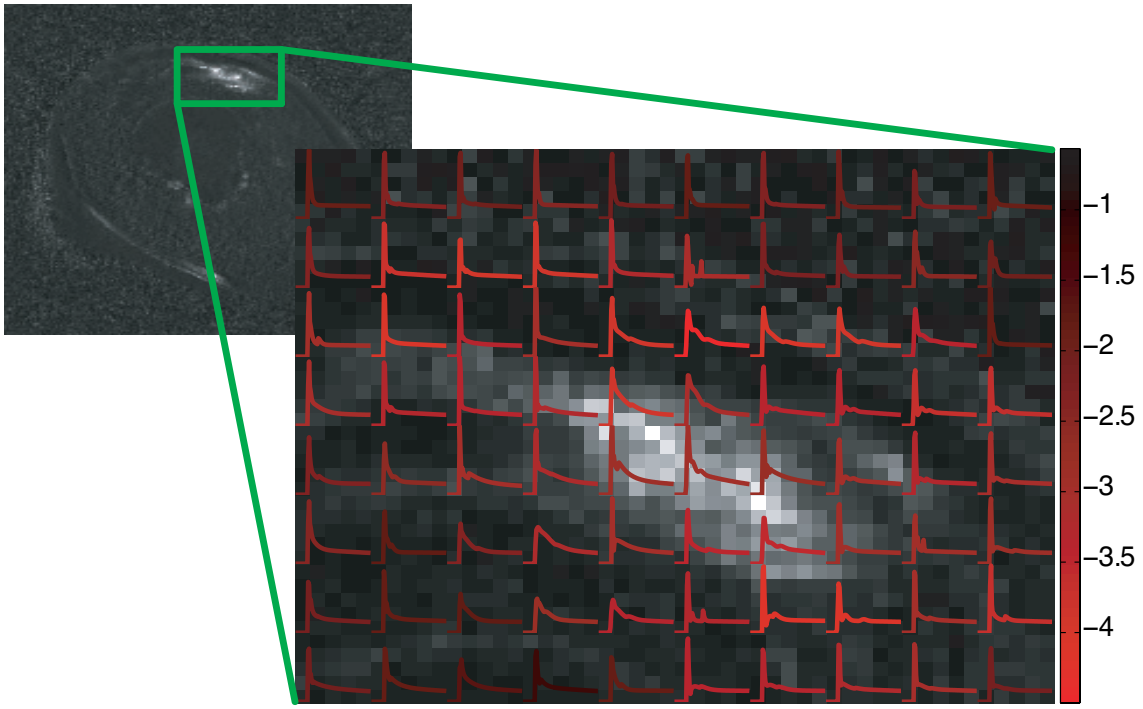

Figure 3.5. Local AIF results. The AMM algorithm was used to estimate an AIF for subsets of tissue concentration curves in a region around a lesion. The patient was scanned near the proximal humerus, with the AIF measured in the brachial artery. The region shown is from a primitive neuroectodermal tumor. The AIFs with the highest confidence based on noise and diversity are found near the center of the tumor. Regions outside the tumor had less signal and diversity. The individual AIFs are color coded based on the relationship displayed in Figure 3.4. The natural logarithm of expected error is shown to increase contrast among the high quality AIF estimations.

to the tumor, which consisted of healthy brain tissue, had AIF estimates that more nearly matched the measured AIF. Dispersion of the AIF within regions of diseased tissue was also evident in the remaining nine datasets not shown here. This suggests that the AIF dispersion was a function of physiology and not the estimation process.

Figures 3.7(a) and 3.8(a) show the kinetic parameter estimates from the measured AIFs for the patients whose local AIFs are displayed in Figures 3.5 and 3.6. Figures 3.7(b) and 3.8(b) show the percent change in the kinetic parameters when the globally estimated AIFs are used in place of the measured AIFs and Figures 3.7(c) and 3.8(c) show the percent change in parameters when the locally estimated AIFs replace the measured AIFs. In Figure 3.7, taken from a neuroectodermal tumor near the proximal humerus, both K^{trans} and k_{ep} decrease across the region with the AMM

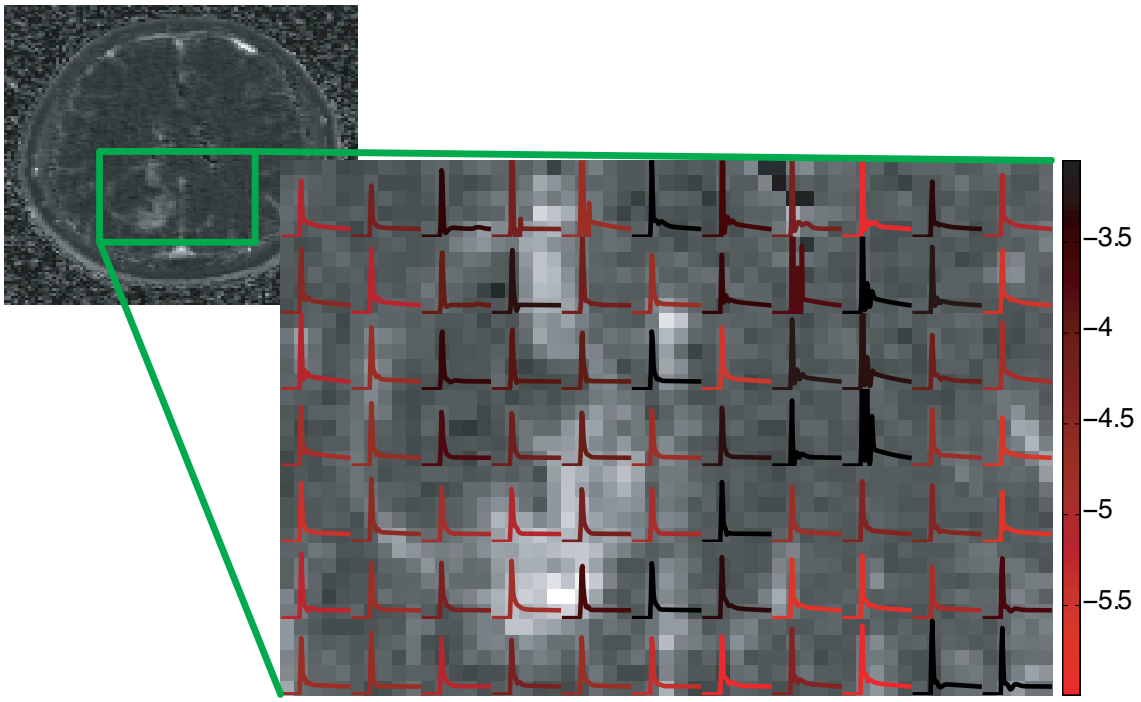

Figure 3.6. Local AIF results. The AMM algorithm was used to estimate an AIF for subsets of tissue curves in a region around a glioma. The patient was scanned at 5 sec temporal resolution. The AIFs with the highest confidence based on noise and diversity are found near voxels with significant arterial signal. In addition, subsets near the center of the tumor also resulted in estimates with high confidence. Regions outside the tumor had less signal and diversity. The individual AIFs are intensity coded based on the relationship displayed in Figure 3.4. The natural logarithm of expected error is shown to increase contrast among the high quality AIF estimations.

method. v_p, on the other hand, increases significantly throughout the lesion.

The opposite trends for K^{trans} and k_{ep} are seen in Figure 3.8, with increases seen throughout the region. When the estimated AIF replaced the measured AIF in Figure 3.8(b), no significant changes in v_p were seen. Use of local AIFs, however, led to a slight increase in v_p across the tumor. The changes in the kinetic parameters are directly related to the changing shapes of the estimated AIFs. As the observed dispersion in the AIF increases, the change in kinetic parameters increases.

The AIC values for the locally estimated AIF model were lower than those from the measured AIF for 10 of the 11 patients in this study. In addition, the AIC values for the globally estimated AIF model were lower than those from the measured AIF for 9 of the 11 patients.

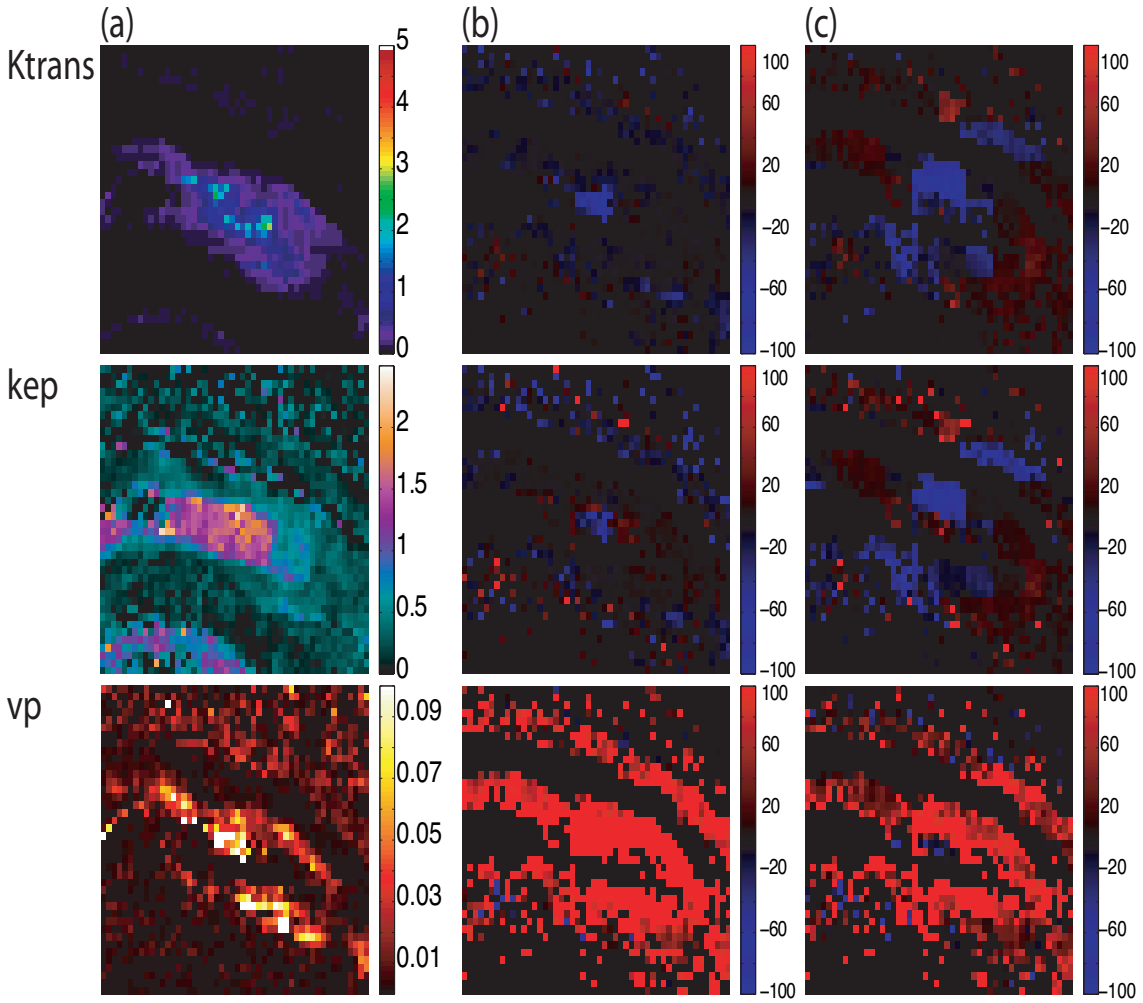

Figure 3.7. Kinetic parameters resulting from the measured AIF (column a), as well as the percent change in parameters when a single AIF was estimated for the whole region (b) and when multiple AIFs were estimated locally across the region (c). Both K^{trans} and k_{ep} decreased across the region, with more significant decreases seen when local AIFs were used (c). v_p increased throughout the region by as much as 200%. These data correspond to the same patient and region seen in Figure 3.5.

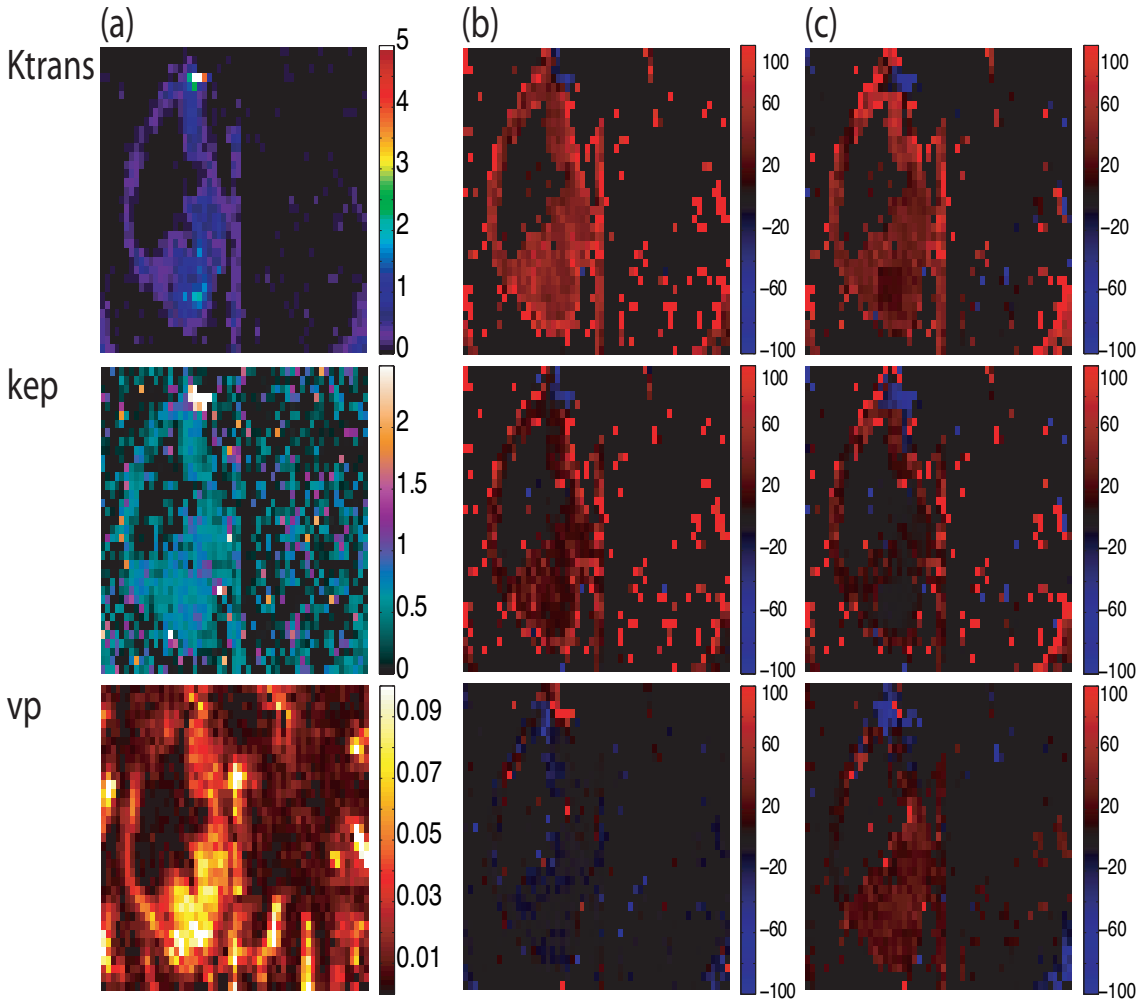

Figure 3.8. Kinetic parameters resulting from the measured AIF (column a), as well as the percent change in parameters when a single AIF was estimated for the whole region (b) and when multiple AIFs were estimated locally across the region (c). Both K^{trans} and k_{ep} increased across the region, with more significant increases seen in (a). v_p increased slightly throughout the region when local AIFs were used (c), but showed no significant change when a global AIF was estimated (b). These data correspond to the same patient and region seen in Figure 3.6.

The changes in kinetic parameters are summarized in Table 3.1. Overall, approximately 32,000 voxels were included in the significance masks from the eleven patients, corresponding to an average of about 600 voxels per slice of data. The parameters from the measured AIFs were compared to those from globally estimated and locally estimated AIFs, and in each case a very close correlation is observed. Figure 3.9 shows a scatter plot comparing the K^{trans} values when the measured AIF was used compared to the local AIFs.

Pearsons correlation coefficient between these parameters is 0.99. In this case, the K^{trans} values from the global AIF tended to be approximately 23% smaller than those from the measured AIF. The lowest overall correlations were between the measured and estimated v_p values. It should be noted again that v_p values tend to be small, on the order of a few percent, and are especially sensitive to poor temporal resolution [**?**]. All of the parameter comparisons were significantly different with two exceptions, k_{ep} differences between the local and global AIFs ($p = 0.12$) and v_p measurements between the measured and local AIFs ($p = 0.56$). In general, K^{trans} and k_{ep} measurements tended to be 9-23% smaller when estimated AIFs were used instead of measured AIFs. This is consistent with the observation that estimated AIFs tend to be dispersed in time with respect to measured AIFs.

Table 3.1. Summary of kinetic parameter correlations and fits with all possible AIF comparisons. Significantly different p-values are denoted with an asterisk.

		K^{trans}			k_{ep}			v_{ep}		
		M-G	M-L	G-L	M-G	M-L	G-L	M-G	M-L	G-L
Linear Fit	Slope	0.91	0.76	0.84	0.87	0.87	0.98	1.04	0.93	0.89
	Intercept	2.73e-4	-4.08e-5	-2.74e-4	0.0024	-0.0010	-0.0022	3.54e-4	2.63e-4	-1.94e-5
Correlation	Pearson's Coefficient	0.99	0.99	0.99	0.97	0.97	0.98	0.97	0.97	0.99
	p-value	0.0053	0	4.4e-11	6.17e-4	7.97e-3	0.12*	3.53e-4	0.56*	3.30e-5

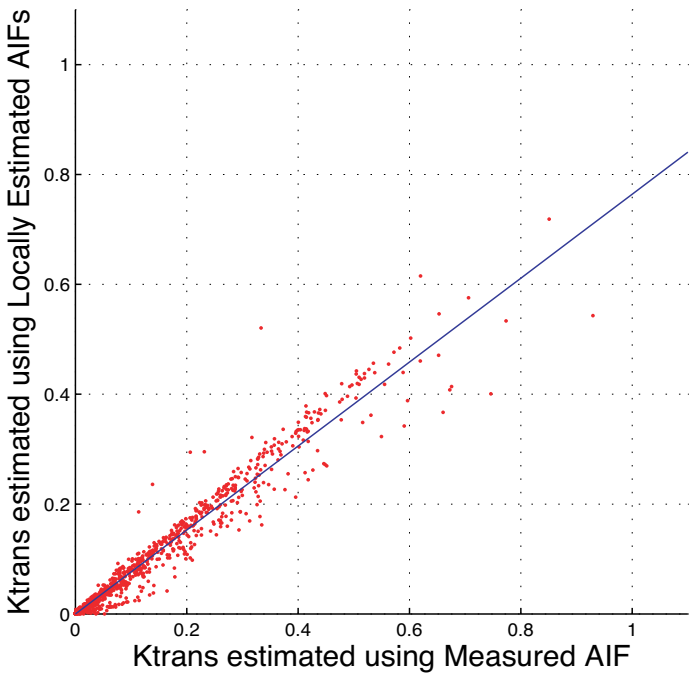

Figure 3.9. Scatter plot of K^{trans} values from all eleven patients. Significance masks were used to extract voxels from regions of interest, resulting in a total of approximately 32,000 voxels. When the measured AIF was used to calculate K^{trans} the values were approximately 23% higher than when locally estimated AIFs were used. A line of best fit is also shown with equation $y = 0.77x - 4.08x10^{-5}$

3.4 Discussion

An increasing number of researchers have noted the detrimental effects of bolus dispersion on accurate quantification of dynamic MR data. Much of this work is focused on bolus dispersion in the brain as part of DSC-MRI studies [**?**, **?**, **?**, **?**]. These methods calculate local AIFs through independent component analysis and through individual voxel screening. The local AIFs are then used to calculate cerebral blood flow (CBF) and other tissue kinetics in the brain. The CBF values found using local AIFs tend to be higher than those calculated with a single, measured AIF. In addition, they have found that the new CBF values have a higher sensitivity and specificity in characterizing stroke, suggesting local determination of the AIF may lead to improved clinical performance. The work presented here demonstrates a different approach to determine the local arterial input function of a region of interest in DCE-MRI scans throughout the body. We have also presented simulated results from which the accuracy of these local AIFs could be determined based on the SNR and diversity in the local tissue curves. This method makes use of the Alternating Minimization with Model (AMM) method described in Chapter 2. Here we expand on that work by examining the changes in the estimated AIF shape across a region of interest in tumors and the effect of local AIF estimation on DCE-MRI parameters.

A similar blind estimation of AIF approach has been carried out by Yang et al. [**?**, **?**]. That work focuses on the use of multiple reference regions to obtain an estimate for the AIF in a region of interest. These estimated AIFs are local to the regions used in the estimation, rather than the neighboring arteries, but are not localized within a reference tissue. Pellerin and others have developed a more elaborate technique incorporating contrast agent diffusion into DCE-MRI [**?**]. This method modifies the Kety model to include a term describing the diffusion of contrast agent between neighboring voxels. The value of the AIF is then estimated at each time point in conjunction with kinetic parameters and diffusion parameters for each voxel, which increases the number of model parameters to be solved. In contrast, the method described in this paper uses a parameterized input function in conjunction with the extended Kety model to limit the number of free parameters in any particular subset containing N clusters to 3N+11. Though the number of

free parameters to be estimated increases with an increasing number of subsets, each individual AIF calculation is computationally efficient, taking an average of 113s (Intel Xeon 2.4 GHz, 8 GB RAM). We take advantage of the fact that each local AIF calculation is independent of the others to estimate local AIFs in parallel (eight at a time with dual quadcore processors, Parallel Computing Toolbox, Mathworks), and obtain linear speedups. Additionally, the blindness of the AMM method allows for increased freedom in selecting imaging parameters by removing constraints on field of view and the dynamic range of signal contrast due to CA injection.

Koutcher and others [**?**, **?**] have investigated the use of population average arterial input functions in quantifying DCE-MRI data. They develop unique population average AIFs for specific arteries, such as the femoral artery, for use in DCE-MRI scans in that area. This work differs from that done previously by Parker [**?**], who developed a more general population average AIF. While these methods have shown some promise in quantifying kinetic parameters they suffer from the same measurement difficulties inherent in all DCE-MRI scans, including those done here, namely partial volume effects, flow effects, and signal saturation effects. Additionally, they are unable to account for interpatient individuality.

The method presented here would allow for data acquisition to be done during a single scan, with concentration dose, flip angle and other parameters optimized to avoid signal saturation in tissue curve acquisition. In addition, local AIF estimation could be used clinically to allow for smaller imaging fields of view, with concomitant increases in spatial resolution. Partial volume and flow effects in arterial voxels are not an issue, as the AIF is estimated without reference to any arterial voxels except as a reference for a global scaling constant as described above. Previous work shows the estimation process to be robust with regards to the initial estimate for the AIF at the SNR/diversity levels used here.

The standard deviation of simulation percent errors was chosen as an error metric because the simulation results did not show any significant bias in kinetic parameter estimates. Also, the simulation results shown in Figures 3.3 and 3.4 represent a scenario in which the entire region of interest consisted of a single type of tissue, here a tumor. Due to the highly heterogeneous nature of tumors, even

relatively small subsets of tumor data contained more than one tissue type, resulting in higher diversity, and thus lower estimation error than a majority of the simulation realizations shown here.

However, there are limitations to the utility of the confidence metric developed here. First, all of the tissue concentration curves used in the simulations are accurately described by the extended Kety model with additive, zero mean Gaussian noise. Though this model is effective at describing tissue concentration data, it does not account for more subtle concentration transport in actual physiology, and so any deviations of the data from the Kety model are not accounted for in the confidence metric. Second, in clinical data, the nonlinear conversion from signal to concentration measurements results in additional error in the concentration measurements of the individual tissue curves [**?**]. In areas of low concentration uptake, these conversion errors often dwarf the actual concentration measurements, resulting in misleadingly high confidences in areas of low concentration uptake. In addition, patient motion, flow effects and other effects also add to concentration error not accounted for in the confidence metric. In practice, the confidence or uncertainty metric developed here would be used in conjunction with errors or uncertainties due to conversion to concentration and the other effects mentioned. These errors could be used to create significance masks that for example screen out voxels with low concentrations, reducing the impact of otherwise high confidences such as those seen in regions of low contrast uptake in Figures 3.5 and 3.6.

Both locally and globally estimated AIFs resulted inK^{trans} and k_{ep} values that were 9-23% smaller than those from measured AIFs. A greater difference in K^{trans} was seen with the local AIFs, and the differences in k_{ep} were nearly identical regardless of the size or location of the estimation input. These differences in kinetic parameters were due in part to the dispersion seen in both the globally and locally estimated AIFs, similar to that reported in Chapter 2. This dispersion is likely due to flow effects as the contrast bolus traverses the vasculature. The lower AIC values resulting from the locally estimated AIFs in 10 of the 11 subjects used in this study suggest that the improvement in model fidelity to the measured data is sufficiently high to warrant the increased complexity of estimating local input

functions. Though absolute truth for the kinetic parameters is not possible to obtain *in vivo*, the improved model fitting suggests that the dispersion and delay seen in the local AIFs, along with the concomitant changes in the kinetic parameters, more accurately reflect the underlying physiology of the tumors.

3.5 Conclusions

Here we presented a method for determining the confidence with which one can blindly estimate a local AIF. This method was used to calculate local AIFs across a tumor region using region grown subsets of varying size with sufficient curve SNR and diversity to allow for a high confidence in the AIF estimation. The resulting kinetic parameters were 9-23% smaller than those estimated with a measured AIF. The differences suggest that the current method of using arterially measured AIFs biases the resulting parameters high, especially in regions where more dispersion in the local blood supply may be expected. Further work is required to quantify the advantages of locally determining the blood supply to a region of diseased tissue with regard to diagnosis and treatment monitoring of disease.

CHAPTER 4

CONSTRAINED ESTIMATION

4.1 Introduction

Dynamic contrast-enhanced (DCE) MRI is a rapidly developing tool for evaluating myocardial perfusion. As with other DCE-MRI applications, measurement of the arterial input function is necessary for accurate tissue quantification. The difficulty of accurately measuring the AIF in cardiac perfusion acquisitions has been widely documented [**?**, **?**, **?**, **?**], and several techniques have been proposed to overcome this difficulty. Among these techniques is the dual bolus method [**?**, **?**, **?**], which measures the AIF and myocardial tissue curves with separate injections of contrast agent of different concentrations. A low concentration dose of gadolinium is used when measuring the AIF to avoid signal saturation effects due to the nonlinear relationship between contrast concentration and signal intensity. A separate acquisition with a high concentration dose is made to acquire the myocardial tissue signal, which maximizes the myocardial signal to noise ratio (SNR). A second class of techniques, referred to as dual acquisition methods [**?**, **?**], use pulse sequences designed to acquire LV blood pool images and myocardial tissue images separately. The LV blood pool images are low resolution, and have short saturation recovery time to minimize signal saturation effects at peak contrast agent concentrations. A third method uses radial acquisition techniques to create subimages with different effective saturation recovery times [**?**, **?**]. These images can be modeled according to the equation in [**?**] to estimate T1 at each time point. These T1 values can then be used to estimate the concentration of contrast.

All of these methods increase the accuracy of AIF measurement for doses high enough to cause significant saturation of the AIF signal. However, these methods also introduce additional complications into the acquisition process. The dual bolus

method doubles the effective imaging time required to obtain perfusion measurements. In addition, physiological variations in the subject between injections may introduce error into the AIF measurement. The dual acquisition method requires imaging an extra slice in each beat. Though relatively brief, this requires nonstandard scanning procedures and cannot be applied retrospectively to previously acquired data. Likewise, the T1 estimation method makes use of special properties of radial acquisitions, and is not applicable to other imaging schemes. Additional research is needed to further validate the dual acquisition and the radial acquisition method. As well, none of the above methods can be applied retrospectively to previously acquired perfusion datasets.

This chapter describes an alternative method for quantifying myocardial perfusion. This method builds upon previous work on blind estimation of the arterial input function directly from tissue concentration curves (see Chapter 2). Blind estimation assumes the tissue concentration curves share a common input function and are related to that input function through a mathematical model. The AIF can then be estimated by iteratively minimizing a cost function associated with the model used. This method has the advantage of only requiring a single scan, with parameters and contrast agent concentrations optimized to obtain maximum SNR in the myocardial wall, and can in theory be applied to any myocardial perfusion dataset in which the tissue curves are not saturated. The purpose of the present study is to adapt the AMM method for use in cardiac perfusion data by using additional AIF information from the nonsaturated portions of the blood pool signal. The resulting constrained AMM (CAMM) model is quantitatively assessed using computer simulations, and preliminary results comparing the presented method with the dual bolus method *in vivo* are presented.

4.2 Methods

4.2.1 CAMM Algorithm

The estimation method developed here is based on the alternating minimization with model (AMM) method presented in Chapter 2. Starting from a set of myocardial tissue concentration curves from a single slice of a myocardial perfusion data set, the

data are spatially upsampled by a factor of two in the x and y directions to aid in the temporal registration of the data, as well as the segmentation. The data are registered temporally and the myocardial tissue is segmented by an experienced observer, using custom software. A conservative segmentation, excluding any voxels from either the LV blood pool or pericardium, was used. The most basal slice was typically selected for estimation, which resulted in approximately 500 myocardial voxels. This slice was selected to match the analysis from the dual bolus protocol (see below), which selects the basal slice for AIF measurement to minimize the impact of flow effects. An unsupervised k-means algorithm was used to classify the tissue concentration measurements into a set of 10 characteristic curves with higher signal to noise ratio (SNR) than the constituent curves themselves. Empirical testing of the minimization algorithm returned nearly identical values over a range of 4 to 20 clustered curves. As 10 clustered curves adequately described the data, that number was used throughout this study. A population average AIF was used to estimate initial kinetic parameter values for each of these characteristic curves in conjunction with an extended Kety model:

$$C_t(t) = K^{trans} e^{-k_{ep}t} \otimes C_b(t) + v_b C_b(t) \tag{4.1}$$

where K^{trans} is the transfer rate constant, k_{ep} is the washout rate constant, v_b is the volume fraction of blood, $\otimes$ represents convolution, $C_b(t)$ refers to the contrast concentration in the blood or AIF and $C_t(t)$ refers to an individual concentration time curve. The population average AIF was taken from the median of 12 resting perfusion scans, each performed with a 0.004 mmol/kg dose of 1/5 concentration contrast agent as part of a dual bolus protocol, detailed below. Previous work with the AMM method without cardiac constraints showed the algorithm to be insensitive to the initial estimate of the AIF within physiologically reasonable bounds.

After the initial kinetic parameters were estimated for each of the characteristic curves, they were held constant and a new AIF was estimated using nonlinear regression. A model parameterization with ten free parameters was used to constrain the shape of the estimated AIF and reduce the impact of measurement noise. The model used was of the form:

$$C_b(t) = \sum_{i=1..3} A_i \gamma_v(\alpha_i, \tau_i, \Delta_i) + A_4 S(\alpha_4, \tau_4, T, \Delta_4) \tag{4.2}$$

where γ_v refers to a gamma variate function and S refers to a sigmoid function [**?**]. In this model A_i are scaling constants, Δ_i are delay terms, α_i and τ_i are related to the shape and width of the first pass bolus and recirculation peaks, and T represents the exponential time constant for contrast elimination from the blood pool. The gamma variate functions represent the first pass of the contrast bolus and subsequent recirculation peaks. The sigmoid function models the rising concentration in the blood due to contrast recirculation. After the parameters describing the initial AIF estimate were obtained, these were held fixed and kinetic parameters were recalculated. The algorithm than continued to alternately refine kinetic parameter and AIF estimates until the change in the mean K^{trans} value between iterations was less than 0.1%.

The AMM implementation used in this chapter differed from previous non-cardiac work by inclusion of an additional constraint on the blind AIF estimate through inclusion of the AIF measured in the LV blood pool along with the tissue concentration curves. The objective function for the minimization process uses Euclidean norms and is written:

$$R = ||\mathbf{C_t}(\mathbf{t}) - \mathbf{H}\vec{C_b(t)}|| + \lambda||w(\hat{L} - \vec{C_b(t)}|| \tag{4.3}$$

where $\mathbf{H}$ is a matrix with the kinetic parameters from the extended Kety model (eq 4.1) that implements a convolution with the AIF $C_b(t)$. $\mathbf{C_t}(\mathbf{t})$ is a matrix holding several (typically 10) clustered tissue curves. $\hat{\mathrm{L}}$ represents the measured LV blood pool signal and λ represents a weight factor. The circumflex over the LV blood pool curve indicates that this curve was assumed to be equal to the true desired AIF only at signal intensities below a threshold where a linear relationship between signal intensity and concentration could be used as a reasonable approximation [**?**]. In this work, it was assumed that the maximum value of the recirculation peak of the measured AIF could be used as a saturation threshold. This threshold was based on previous work done with the dual bolus method and is specific to the dose and sequence used here. w implements this threshold by being 0 above the threshold and 1 below. While previous work with the AMM method required an independent

measurement of blood pool contrast concentration to eliminate ambiguity in the scaling of the estimated AIF and kinetic parameters, the inclusion of the LV blood pool signal eliminates this ambiguity by constraining the value of the estimated AIF at low concentrations.

4.2.2 Simulations

Computer simulations were used to test the ability of the CAMM method to accurately estimate AIFs and kinetic parameter values. A particular concern was that the diversity of tissue curves in healthy heart tissue might not be sufficient to enable robust AIF estimation as the matrix to be minimized will become singular or nearly singular. Work on related AIF estimation algorithms has shown that diversity in kinetic parameters leads to improved estimation quality (see Chapter 3) [**?**]. To ensure realistic simulations, a pool of kinetic parameters was collected from a set of myocardial perfusion DCE-MRI data sets acquired using the dual bolus method as described below. Parameters were calculated voxelwise using the low dose AIF. Histograms of the pooled kinetic parameter estimates are shown in Figure 4.1. The individual parameter histograms from each subject had similar means and distributions, which implies that it is reasonable to draw from the entire pool to create simulations. A true AIF was created by fitting the AIF model given by equation 4.2 to the low dose dual bolus AIF from one of the perfusion scans.

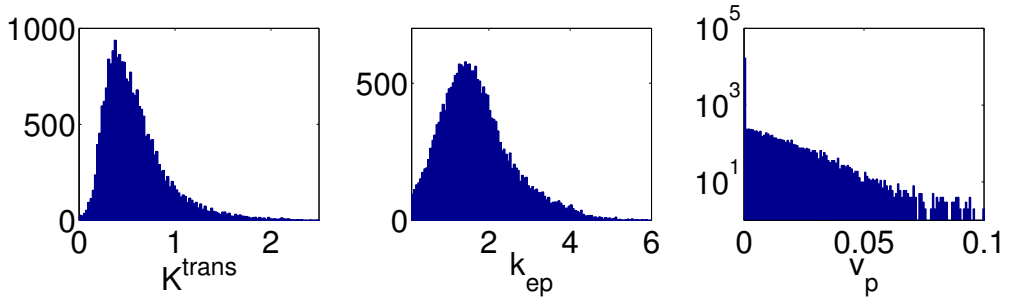

Figure 4.1. Histograms of the kinetic parameters collected from twelve subjects. These parameter sets were used in the computer simulations described here. The v_b values are shown on a logarithmic scale to highlight the distribution in parameters. The means and distributions were consistent for each of the data sets from which these pools were created.

This model fitting was done to remove measurement noise from the 'true' AIFs for the simulations. For each realization, five hundred sets of kinetic parameters were randomly selected from the pool and tissue curves were created according to equation 4.1. Zero mean Gaussian noise was added to each of the tissue curves independently. The standard deviation of the noise was 5% of the maximum value of the tissue curves, roughly corresponding to the average noise value in the twelve data sets. Example simulated tissue curves, as well as sample tissue curves from the *in vivo* data are seen in Figure 4.2. The five hundred curves, corresponding to the average number of myocardial tissue curves in a single slice of a perfusion scan, were then clustered into 10 curves. Example cluster averaged curves from *in vivo* data are seen in Figure 4.3. The 10 cluster averaged curves were input to the CAMM algorithm along with the 'true' AIF signal clipped at the maximum value of the recirculation peak as described above and the resulting estimated AIF used to calculate kinetic parameters for each of the original tissue curves. The relative and absolute errors for each of the five hundred sets of kinetic parameters were then tabulated and the median errors were determined. 1000 realizations were conducted using the same true AIF, and five true AIFs based on five of the human studies were used for a total of 5000 noise realizations. The five 'true' AIFs were selected to cover a range of reasonably expected input functions, including total acquisition time. The second simulated AIF was selected to represent a short acquisition, approximately 26 seconds

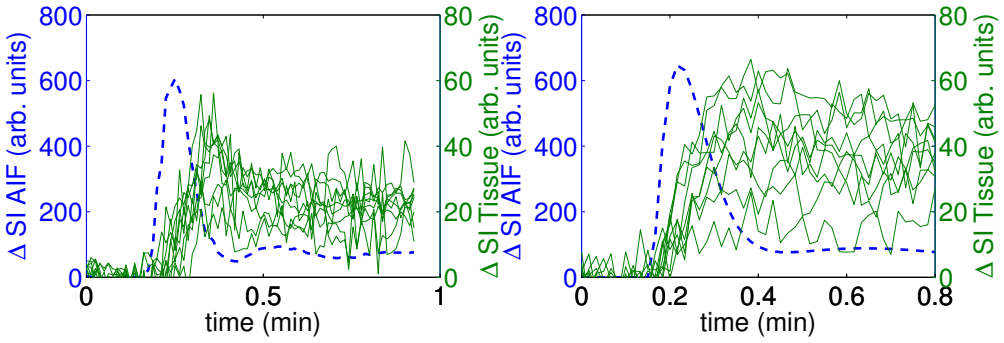

Figure 4.2. Sample AIFs (dashed line) and voxelwise, spatially upsampled tissue curves from subject data (effective in plane resolution of 1.2X1.2mm) (a) and from the computer simulation (b).

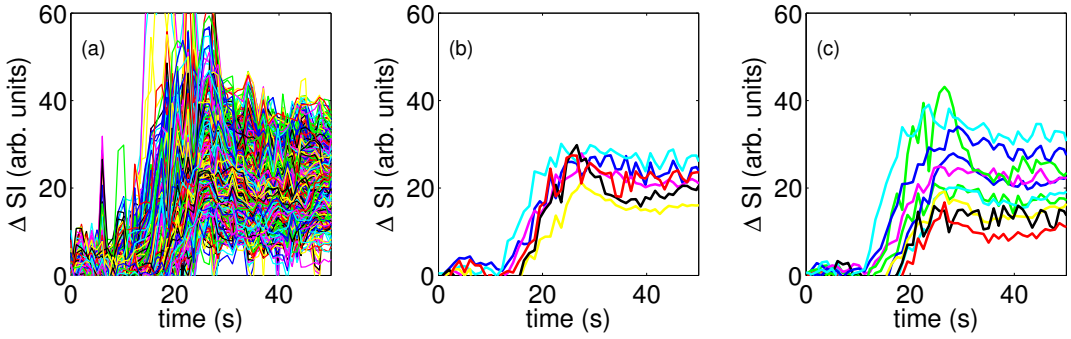

Figure 4.3. Sample myocardial tissue curves collected voxelwise (a), averaged into six equiangular regions (b), and from the k-means cluster averaged curves (c). Cluster averaging yield higher diversity representative curves with respect to region averaging.

following contrast uptake in the LV.

4.2.3 Subject Data

The CAMM method was also applied to resting myocardial perfusion data sets from 21 subjects, 8 female and 13 male with mean age 49±14 years (range: 26-70), mean weight 85.5±21.6 kg (range: 59-123). Each of the subjects volunteered to be scanned as part of IRB approved ongoing research studies. Though the subjects in this study were not screened for coronary artery disease, two of the subjects studied here had been previously diagnosed with coronary artery disease. A dual bolus protocol was used in which subjects were first injected with a low dose (0.004 mmol/kg) of dilute (1/5 concentration) Gd-BOPTA contrast, followed by a higher, nondilute dose (0.02 mmol/kg). Both injections were followed by a 25 mL saline flush, and both contrast and saline were injected at a rate of 5 mL/s by power injector (Medrad Inc., Indianola, PA, USA). All acquisitions were done at 3T, with Siemens Verio and Trio scanners (Siemens Medical Solutions, Erlangen, Germany). A saturation recovery, radial turboFLASH sequence was used with 72 interleaved rays over 180 degrees, TR/TE = 2.6/1.4 ms, flip angle of 14°, slice thickness of 8 mm, and isotropic in plane resolution of 2.3 mm. An iterative, constrained reconstruction method was used to reconstruct the images offline [**?**]. Each time frame was manually registered to account for respiratory motion and the myocardial tissue was segmented manually

by an experienced observer. The mean precontrast signal was subtracted from the data to obtain relative signal changes (which introduces additional uncertainty). AIFs were determined for both low- and high-dose scans from a region of interest in the LV blood pool. True AIFs, determined from the low-dose AIF scaled by 5, were used to determine true kinetic parameters for each of the myocardial voxels in the higher dose scan. An independent delay term was included for each tissue curve in the fitting process to account for differences in uptake time between the dual bolus and estimated AIFs and the tissue curves.

AIFs were also estimated using the CAMM algorithm for each of the 21 subjects. Myocardial tissue concentration curves were collected from a single, relatively basal slice from each 0.02 mmol/kg dose scan and input into the algorithm as described above. The resulting AIF estimate was used to compute kinetic parameters voxelwise in each subject. The percent difference in the area under the curve (AUC) of the first pass of the estimated and dual bolus AIF, as defined by the first gamma-variate curve in the model fit to the data, was calculated for each patient. The myocardium was then divided into six equiangular regions and the parameters in each region were averaged to obtain six sets of parameters per subject. Independent, two tailed t-tests were performed to compare the parameters resulting from the CAMM method and dual bolus method. Linear regression was used to determine the relationship between parameters from the dual bolus and estimated AIFs.

Following data acquisition at rest, a second set of dynamic images was acquired for eight of the subjects during adenosine infusion (140 μg/kg/min). A single higher, nondilute dose (0.03 mmol/kg) of contrast was injected, followed by a 25 mL saline flush. These images were reconstructed and processed using the same protocol as was used at rest. The CAMM method was used to estimate an AIF for each subject and pharmacokinetic parameters were calculated voxelwise and then averaged in each of six equi-angular regions, as in the resting studies. No reference standard was available; this analysis was performed to determine if the method gave reasonable results when a higher dose and stress were used.

4.3 Results

4.3.1 Simulations

Figure 4.4 shows histograms of the median absolute error in each of the 5000 noise realizations for each of the three kinetic parameters from the pooled results of the computer simulations. The K^{trans} errors range from -0.19 to 0.02, with a median error of -0.004. The histogram of K^{trans} errors has two distinct local maxima, one centered at 0.0 error and one centered at -0.04 error. The majority of the realizations comprising the second maximum arose from the set of noise realizations using the true AIF with the shortest total acquisition time. This can be seen further in Figure 4.5, which displays joint probability density functions for K^{trans} estimates for the cardiac AMM and dual bolus methods. The values resulting from the set of simulations with the shortest total acquisition time (Figure 4.5(b)) have a higher bias than those from the other four sets. The errors in k_{ep} range from -0.32 to 0.08, with a median error of 0.0. The k_{ep} errors are unimodal and negatively skewed. v_b errors were much smaller than those for either K^{trans} or k_{ep}, with a range of -0.004 to 0.0 and a median value of -0.0003. The errors for v_b followed the same trends as those for K^{trans}, with the small peak in the histogram also due to bias in the set of realizations with a short acquisition time.

The five AIFs used in the simulations are shown in Figure 4.6. The minimum

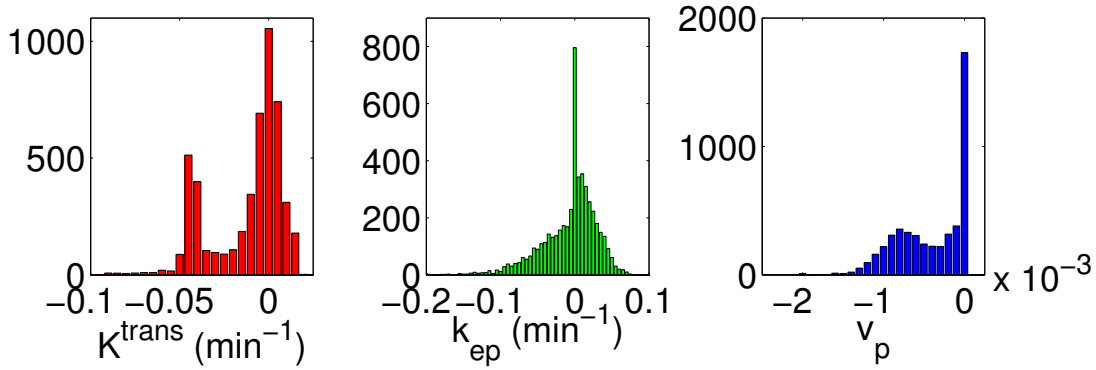

Figure 4.4. Histograms of the error for the computer simulations. The second peak in the K^{trans} errors results mostly from one of the five sets of 1000 simulations, as seen in the joint PDFs in Figure 4.5. This set of simulations had the shortest overall scan time of 0.55 min.

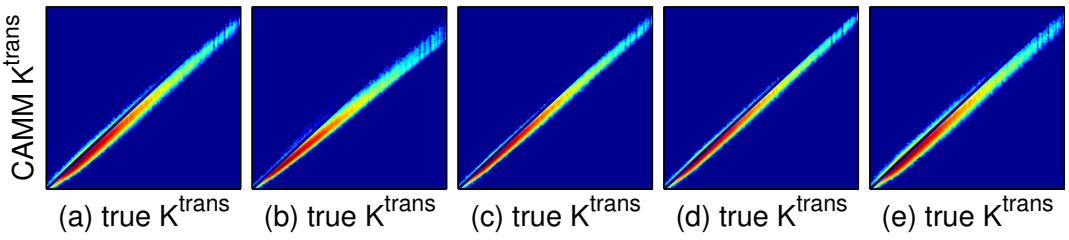

Figure 4.5. Joint PDFs of the CAMM estimates for K^{trans} vs. true values, plotted on a logarithmic color scale, for the noise simulations.

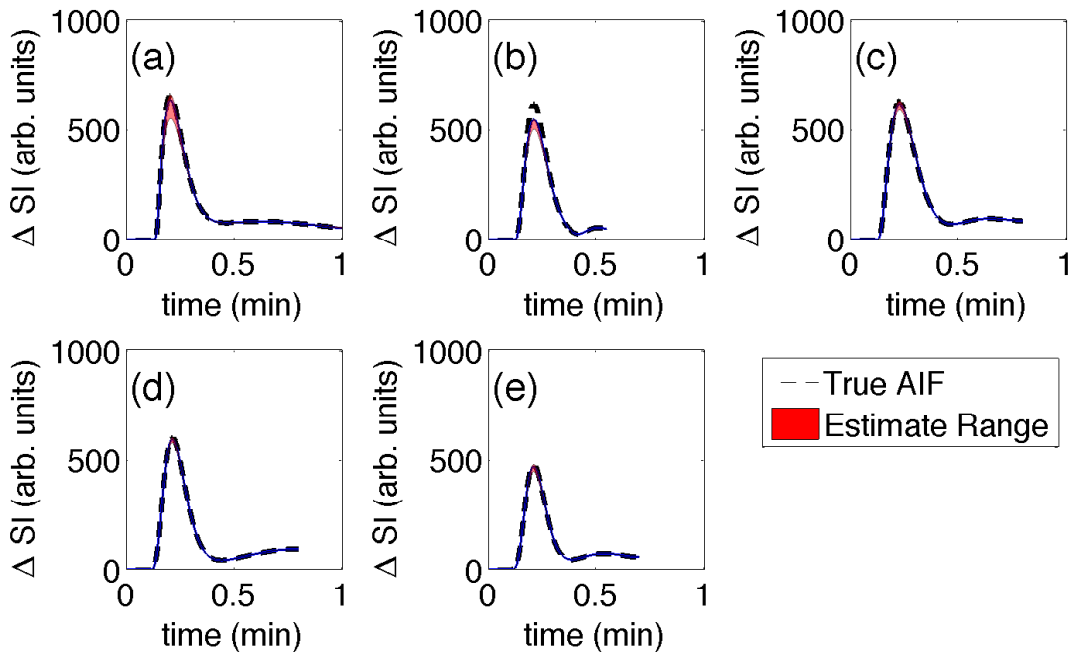

Figure 4.6. AIFs from the computer simulations. The dashed lines represent the five true AIFs used in the simulations. The red area represents the full range in the estimated AIFs, and the blue line represents the median estimated AIF. In all five cases, the median was near the top of the range of estimated AIFs (which were not normally distributed).

and maximum estimated AIFs in each case are shown, along with the median AIF from all the noise realizations using that AIF. The second, smaller grouping of errors seen in K^{trans} and v_b in Figure 4.4 both arose from the second AIF in the simulation set. This AIF had the shortest simulated total acquisition time of the AIFs tested here at approximately 33 seconds (26 seconds of nonzero data).

4.3.2 Subject Data

Data of acceptable quality was obtained in 20 of the 21 subjects in this study. The one subject was eliminated due to insufficiently long acquisition time. The simulation results shown above suggest that acquisitions that do not fully sample the recirculation peak result in higher error compared to longer acquisitions, and thus the one scan with an incomplete recirculation peak was excluded from the study. Figure 4.7 displays the AIFs from the *in vivo* data tests for the twenty subjects. The peak change in signal intensity (ΔSI) of the full dose AIF ranged from 37% to 100% of the dual bolus AIF ΔSI peak height, due to signal saturation as the contrast agent bolus made its first pass through the LV blood pool. The estimated AIFs from the CAMM method are overlaid with the measured AIFs and the percent difference in the first pass AUC are displayed. The changes in the AUC ranged from 0% to 38%. Due to the constraint imposed by the inclusion of portions of the full dose blood signal in the estimation process, the estimated AIFs are strongly affected by the constraint of the full dose AIFs below the maximum of the recirculation peak. The low dose portion of the dual bolus AIFs was acquired in a separate scan several minutes prior to the full dose scan, and changes in patient physiology and motion between scans account for the differences in uptake time and bolus width seen in Figure 4.7.

K^{trans} estimates were not significantly different for 17 of the subjects ($p > 0.05$), but were significantly lower for the other three ($p = 0.02, 0.004, 0.000$, mean absolute difference of 0.18, 0.15, 0.94). k_{ep} estimates were not significantly different for 15 subjects, but were significantly different for the other five (p =0.000, 0.003, 0.004, 0.001, 0.000). v_b was not significantly different for 12 subjects, but was significantly different for the other eight (p =0.03, 0.003, 0.004, 0.04, 0.03, 0.001, 0.003, 0.000).

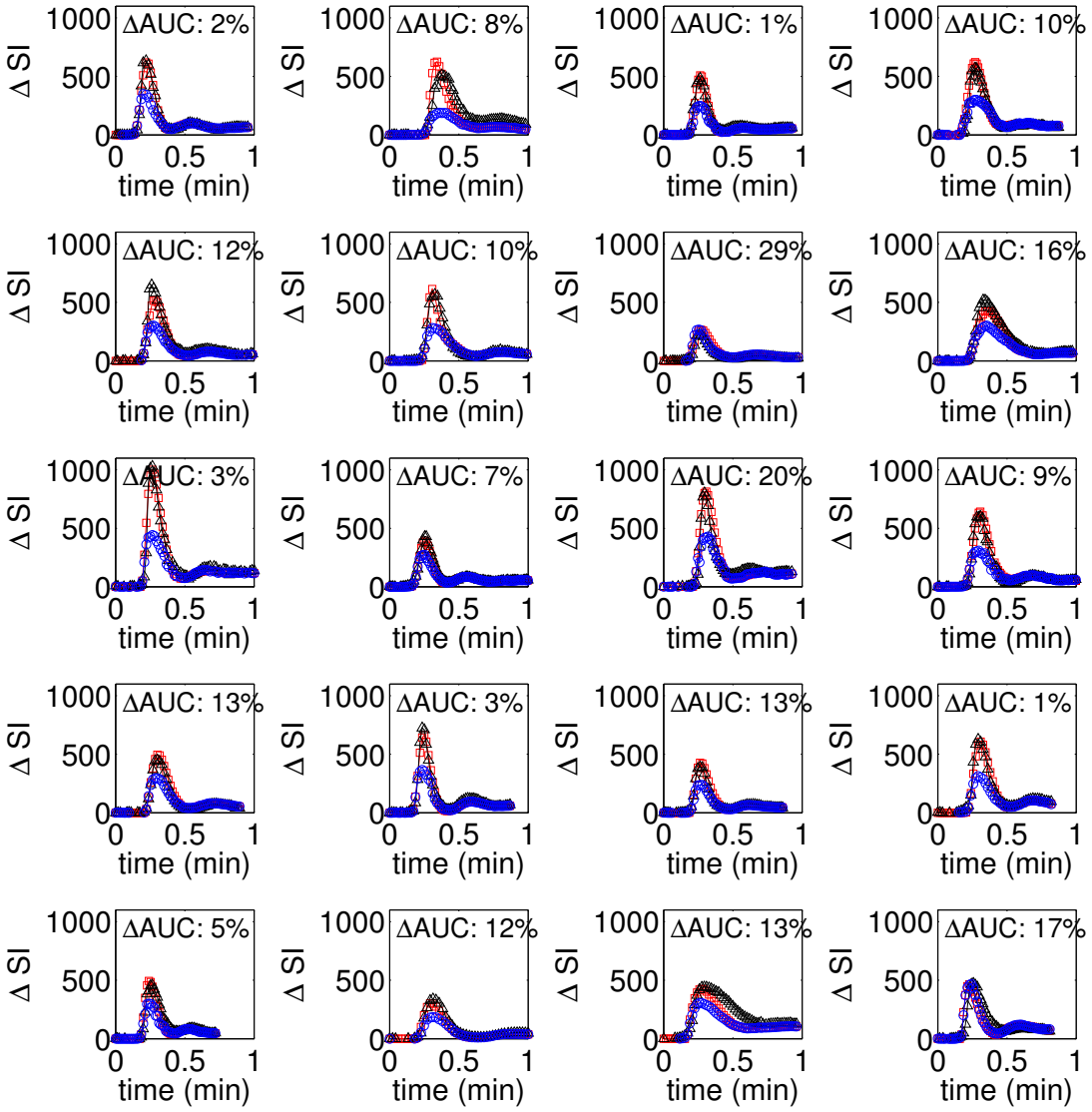

Figure 4.7. Dual bolus and estimated AIFs from 20 patients. The CAMM estimated AIF is shown in red (squares), and the dual bolus AIF is shown in black (triangles). In each case, the directly measured LV blood pool signal is also shown for comparison in blue (circles). The percent differences in the AUC of the first pass of the dual bolus and CAMM AIFs are also shown. The dual bolus AIFs were acquired 3-7 minutes before the full dose measured AIFs.

Overall, the average parameters from the two methods were not significantly different (p = 0.450.690.52 for K^{trans}, k_{ep}, v_b respectively). Figure 4.8 displays scatter plots of the region averaged parameters. K^{trans} values for these subjects have a close correlation ($r^2 = 0.89$) with a linear fit of K^{trans} (CAMM)=0.95 K^{trans} (dual bolus) +0.04. The correlation for k_{ep} was equal to that for K^{trans} ($r^2 = 0.89$) with a linear fit of k_{ep} (CAMM)=0.73 k_{ep} (dual bolus) + 0.50. v_b has a slightly worse correlation ($r^2 = 0.82$) and a linear fit of v_b (CAMM)=0.68 v_b (dual bolus) +0.00. Figure 4.9 shows the estimated AIFs for the eight subjects imaged during stress. In each case the signal from the LV blood pool is also shown. The mean K^{trans} values for the eight subjects were 209% higher at stress than at rest.

4.4 Discussion

This chapter presents a new method for determining the arterial input function for use in myocardial perfusion quantification. This method builds upon the previously reported alternating minimization with model (AMM) method (see Chapter 2) by incorporating additional information regarding the AIF from the measured LV blood pool signal.

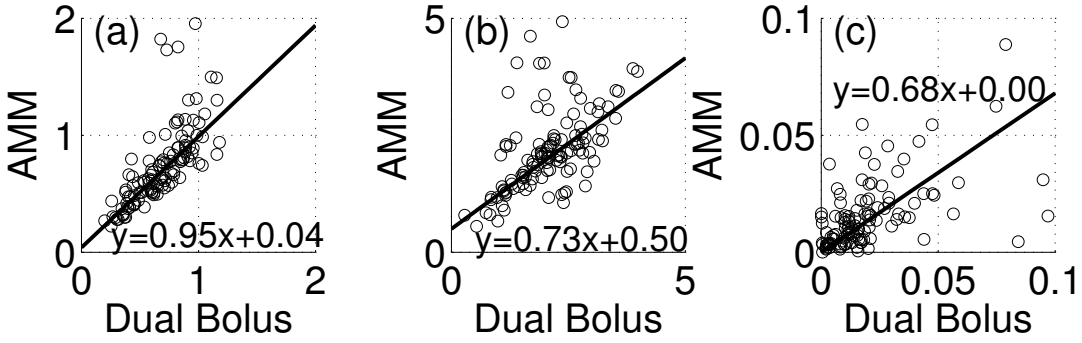

Figure 4.8. Scatter plots of the six region wide averages for the kinetic parameters for each of the 20 subjects from the *in vivo* data. K^{trans} estimates (a) had a good linear correlation with K^{trans} values from the dual bolus method. k_{ep} (b) and v_b (c) estimates had lower correlations due to differences in bolus width between the estimated and dual bolus AIFs. The lines of best fit are also shown in black.

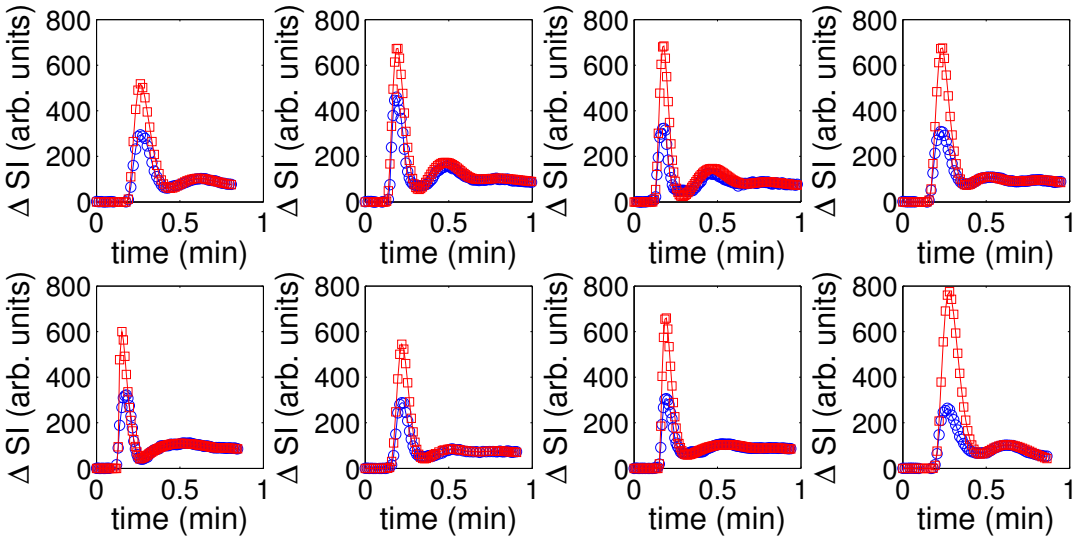

Figure 4.9. Measured and estimated AIFs from eight stress acquisitions. The CAMM estimated AIF is shown in red (squares), and the directly measured LV blood pool signal is shown in blue (circles).

Several AIF estimation methods have been developed for use in DCE-MRI with applications to various types of cancer [**?**, **?**], or in dynamic PET studies [**?**]. Unlike DCE-MRI data in tumors, myocardial DCE data tend to have lower diversity among tissue uptake curves, higher temporal resolution, and sharper AIFs with significant saturation even at relatively low contrast doses. A lack of other candidate reference tissues with input functions identical to those of myocardium makes reference region approaches impractical for myocardial imaging. The diversity of tissue kinetics in healthy myocardium may be insufficient for other blind estimation techniques [**?**, **?**]. Increase heterogeneity in the tissue curves input to the estimation algorithm increases the ability of the algorithm to reliably estimation the AIF (see Chapter 3). This makes maximizing the diversity of the myocardial perfusion curves a desirable goal. The k-means clustering strategy described above yields tissue curves with greater diversity than spatial averaging (such as with six equiangular regions), as seen in Figure 4.3. Although diversity by multiplicative scale factors is not helpful for the CAMM algorithm, this can be considered an additional advantage. That is, scale differences in the tissue curves due to coil sensitivity variations will not affect the estimate of the AIF. In addition, the majority of the subjects used in this work

were volunteers with no known cardiac disease. It is possible that the algorithms performance would be expected to improve with data from patients with disease and correspondinly increased heterogeneity in tissue characteristics, though this requires further study.

The results from the computer simulations (Figure 4.4) show that the median errors in the kinetic parameters when the CAMM method is used are near zero for K^{trans} and k_{ep} when the acquisition time is approximately 1 minute. The errors and the estimated AIFs (Figure 4.6) both suggest that the CAMM method may exhibit some bias and slightly underestimate the peak values of the AIF when the acquisition time is shorter. This underestimation should not be attributed to the AIF model used, as that model describes the simulated AIFs. We hypothesize that the AMM method is sensitive to the total acquisition time. The simulation with the second simulated AIF (Figure 4.4) was repeated with a longer simulated acquisition time ($t = 1.5min$) and gave less bias, with results comparable to the other simulations. In addition, two *in vivo* data sets were artificially truncated after 30 seconds of acquisition and the estimation was repeated with this truncated data. In both sets, the agreement between the estimated and dual bolus AIFs worsened as a result of the data truncation, with the CAMM method consistently underestimating the AIF with respect to the dual bolus AIF. Further research is required to fully characterize the relationship between estimation quality and total acquisition time. However, the poor estimation quality in both simulation and *in vivo* data suggest that insufficient washout information in the tissue curves leads to non-unique AIF/kinetic parameter combinations in fitting the models to noisy tissue curves. For the data here, 1 minute of data provided good estimates of the AIF.

In this implementation the AIF estimation was constrained to be similar to the saturated LV blood pool signal below a threshold. While the AMM method without a constraint worked for a subset of the cardiac datasets, the unconstrained results were poor in a number of cases. The portion of the LV blood pool signal to use as a constraint was that for which the relationship between signal change and concentration is approximately linear. This value was selected based on comparison of low-dose and high-dose AIFs from dual bolus studies for the concentration dose and

imaging protocol used here. In practice the user would need to select a conservative threshold determined by the imaging parameters and dose employed.

One potential limitation of this study is the population average AIF used to initialize the CAMM estimation. This population average was taken from a subset of 12 patients from the dual bolus AIFs measured here. Previous work with the AMM algorithm in sarcoma patients showed that the estimation performance was insensitive to the initial AIF selection within physiologically reasonable bounds (see Chapter 2), however more work is needed to test the CAMM algorithm presented here with patients whose AIFs are significantly different from the population average. A second limitation of the work presented here is the lack of coil sensitivity correction. As mentioned above, the CAMM method is insensitive to the scaling of the input tissue curves. However, more accurate absolute parameter values can be obtained when the tissue and blood regions are corrected for coil sensitivity.

Small but statistically significant differences in the K^{trans} parameter were seen in three of the twenty subjects studied here. These differences may be due to problems inherent in the dual bolus protocol employed here. Despite careful efforts to maintain consistent protocol between the low and high concentration injections, variations in patient physiology, including the effects of respiratory variations on venous return and fluctuations in heart rate, may adversely affect the dual bolus AIF. Among the subjects studied here, the average change in heart rate between the low and high dose scans was less than one beat per minute; however, three of the volunteers' heart rates changed by more than four beats per minute. In addition, flow effects in the LV blood pool affect the observed signal changes in the dual bolus protocol [**?**]. Flow effects will be less severe in the CAMM method, which only makes use of the LV blood pool signal as an additional constraint on the AIF shape after the first bolus pass. Conversely, the CAMM method as used here does not account for any signal saturation in the myocardial tissue curves themselves. If the linear approximation between change in signal intensity and contrast agent concentration in the myocardial tissue curves is not valid, those errors will propagate through the AIF estimation. With the contrast dose studied here, no signal saturation in the tissue curves is expected.

K^{trans} values resulting from the estimated and dual bolus AIFs had a high ($r^2 = 0.89$), linear correlation. The K^{trans} parameter is directly related to myocardial blood flow, and has been shown to not be significantly different from flow estimated with model independent analyses [**?**]. The ability of the CAMM method to replicate K^{trans} measurements suggests that this method may find use in quantitative myocardial flow measurements [**?**].

In conclusion, the CAMM method presented here provides a way to quantify myocardial tissue perfusion with a single injection of gadolinium when the measured AIFs have peak saturation on the order of 30-70%. The method likely works with a wide range of standard, easily implemented acquisitions. Though further work assessing the range of saturation for which this method is successful is needed, the cardiac CAMM method currently provides reasonable estimates for the kinetic parameters and could be used with future myocardial perfusion studies to simplify scanning protocols. The subject data presented here was from resting perfusion scans. At stress, the AIF shape is similar to the resting AIF, and the algorithm may perform equally well. Further testing is needed to verify the application of the CAMM method to stress perfusion scans. Further testing will also focus on the ability of the CAMM method to accurately return kinetic parameters in populations with known or suspected coronary artery disease. In addition, it may be possible to apply this method retrospectively to existing myocardial perfusion data that previously could only be analyzed qualitatively, as well as to dynamic PET or CT studies using similar compartmental model analysis.

CHAPTER 5

TEMPORAL SAMPLING

5.1 Introduction

DCE-MRI has been shown to provide high sensitivity and moderate specificity in detecting breast cancer (see reviews [**?**, **?**]). In addition, changes in tumor volume as measured with DCE-MRI have been shown to correlate well early pathological response to chemotherapy [**?**, **?**]. Many methods for analyzing breast DCE-MRI data have been proposed. These methods include qualitative assessment of morphological features; semiquantitative parameters such as signal enhancement, contrast wash-in and wash-out rates; and quantitative pharmacokinetic modeling (see references in [**?**]). In addition, more recent analysis techniques such as fuzzy c-means clustering [**?**], principal component analysis [**?**], and textural kinetics [**?**] have been proposed for automatic identification of breast lesions. Selecting an optimal analysis method remains an open question. This chapter focuses on two more commonly used techniques for classifying lesions with DCE-MRI, the semiquantitative three time point (3TP) method [**?**, **?**, **?**, **?**, **?**, **?**] and the fully quantitative extended Tofts-Kety (ETK) two compartment model [**?**, **?**, **?**, **?**].

The question of whether to use a semiquantitative model, like the 3TP method, or a quantitative model, such as the ETK method is highly influenced by the temporal sampling rate of images being acquired. Increasing the spatial and temporal resolution of the MR acquisition both result in decreasing the SNR of the acquired images, so a balance between competing demands must be made. Images with high spatial resolution are well suited for qualitative assessment of areas with contrast uptake and washout and are often used to segment breast lesions into fine heterogeneous structures. Quantitative analyses, on the other hand, require higher temporal sampling rates than the semiquantitative methods. These quantitative methods fit

mathematical models to measured data, and rapid sampling of the data is required for good model fidelity. The rate at which tissue curves should be sampled is an area of active research and depends on the particular model implementation chosen [**?**, **?**]. The ETK model studied here requires knowledge of the contrast input to the tissue, known as the arterial input function (AIF). In many applications, the AIF varies more rapidly in time than tissue curves, and the limits on temporal sampling are driven by the AIF. Henderson suggests that accurate quantitative of tissue parameters requires sampling the AIF once per second. Tissue concentration curves, on the other hand should be sampled at least every four seconds to obtain accurate information on the fractional plasma volume (v_p) in the tissue [**?**].

Another issue for analyses using the ETK model with breast DCE-MRI involves the accurate acquisition of the AIF. Automatic detection techniques have been proposed for selecting the AIF from the breast DCE-MRI data [**?**]; however, due to the relatively small size of the axillary artery, the measurements may suffer from partial volume effects [**?**]. Population average input functions have also been proposed [**?**, **?**] though these are necessarily limited in their response to interpatient variation. Other work has been performed on a blind estimation method for determining the AIF directly from measure tissue enhancement curves (see Chapter 2). The blind estimation approach uses a parameterized form for the AIF to minimize the impact of measurement noise. In addition, the estimation can be done at an arbitrarily high sampling rate, alleviating some of the constraints inherent in quantitative modeling.

This chapter aims to compare the quantitative ETK analysis method to the more commonly used 3TP semiquantitative analysis. The alternating minimization with model (AMM) algorithm is used to estimate the AIF for use with the ETK method. Computer simulations are used to investigate the ability of the ETK model to accurately return pharmacokinetic parameters at various temporal resolutions. The blind estimation implementations are done at one second temporal resolution, consistent with the recommendations of Henderson et al. These simulations also test the ability of the 3TP model to accurately return semiquantitative parameters at various temporal sampling rates. Both the ETK and 3TP models are applied to previously acquired breast DCE-MRI data with pathology proven lesions. The

diagnostic utility of the respective methods will be determined as a function of the temporal sampling rate of the acquired data.

5.2 Methods

5.2.1 Three-time-point Method

The 3TP method used in this work is based upon previously published work [?, ?, ?, ?]. This method is a parametric description of individual tissue curves that assigns each voxel in the image a color (red, green, or blue) and color intensity. Three samples or time points from each time curve are considered. The time points used here are one time point precontrast, one 2 minutes following contrast injection, and one 6 minutes following contrast injection. The intensity of the color of each voxel is directly related to the relative change in signal intensity between the first and second time points, and reflects the rate at which the contrast agent is initially taken up into the voxel. The color of each voxel is related to the relative change in signal intensity between the second and third time points. Voxels with at least a 10% increase in signal enhancement are colored blue, voxels whose signal enhancement changes by less than 10% are green, and voxels with a 10% or greater decrease in signal enhancement are colored red. A calibration map is used to ensure consistency across images [?, ?]. 3TP analysis is typically done with data acquired with a 1-2 minute temporal sampling rate [?, ?, ?].

5.2.2 Extended Tofts-Kety Model

The extended Tofts-Kety model is a compartmental model that describes the tissues being imaged as a mixture of two compartments into and out of which the contrast agent can flow. Mathematically, the ETK model is given as:

$$C_t(t) = K^{trans} e^{-k_{ep}t} \otimes C_p(t) + v_p C_p(t) \tag{5.1}$$

where K^{trans} is the transfer rate constant, k_{ep} is the washout rate constant, v_p is the volume fraction of blood plasma, $\otimes$ represents convolution, $C_p(t)$ refers to the contrast concentration in the blood plasma or AIF and $C_t(t)$ refers to an individual concentration time curve. A separate parameter, v_e, represents the extracellular

volume fraction, and is equal to the quotient of K^{trans} and k_{ep} (derivation of this model and explanation of standardized parameters given in [**?**]).

In this chapter, tissue concentration curves were calculated from the signal enhancement data by numerically solving the nonlinear relationship between signal and concentration [**?**]. This method minimizes the impact of concentration measurement error due to signal saturation. A functional representation of the AIF was used in this implementation, consisting of three gamma variate curves and a sigmoid curve. The alternating minimization with model (AMM) method was used to blindly estimate an AIF directly from the tissue concentration curves (see Chapter 2 for details). Briefly, this method estimates the AIF by minimizing a cost function based on the ETK model. A functional form for the AIF is used to reduce the number of parameters to be estimated, as well as to reduce the impact of measurement noise on the estimation. ETK model parameters are then found using the estimated AIF and a linearized form of equation 5.1 for speed [**?**].

5.2.3 Temporal Resolution Simulations

Computer simulations were done to assess the effect of temporal resolution on both the ETK and 3TP models. These simulations were based on previously acquired patient data. Seventy-five lesions were simulated according to the following strategy:

1. Kinetic parameters were determined from a region of interest defined around a lesion from a breast DCE-MRI scan using a population averaged AIF.

2. A 'true' AIF was created by dispersing a population averaged AIF with a Gaussian kernel. The width of the Gaussian kernel was a randomly selected value between 0 and 0.2 minutes. This dispersion was included so that the true AIF would not necessarily be equivalent to the population average. Sample dispersed AIFs can be seen in Figure 5.1.

3. 'True' tissue curves were created according to equation 5.1 using the 'true' AIF and the lesion kinetic parameters. These curves were created with one second temporal resolution and eight minutes simulated acquisition.

4. 'True' 3TP parameters were calculated for each of the tissue curves.

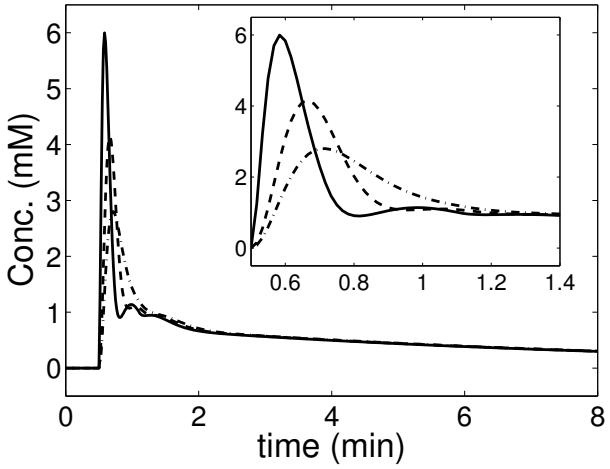

Figure 5.1. Three sample AIFs used in the temporal resolution simulations. The first AIF (solid line) represents the population average AIF. The dashed AIFs represent AIFs dispersed with kernels of width 0.1 and 0.2.

5. Zero-mean Gaussian noise with standard deviation of 0.03 mM was added independently to each true tissue curve. This noise level was the average noise level found in the lesions on which the simulations are based.

6. Each tissue curve was down sampled to 4, 8, 16, and 32 second temporal resolution. This downsampling was done by averaging every 4^{th}, 8^{th}, 16^{th}, and 32^{nd} point from the true curves. This type of downsampling reflects the higher SNR that would be achievable with lower temporal resolution imaging.

7. Parameters were calculated using an AIF obtained from the AMM blind estimation method developed previously for use with the ETK model. The noisy tissue curves were upsampled to 1 second resolution with cubic interpolation. The AIF was estimated with 1 second resolution, and the kinetic parameters were calculated with the upsampled AIF and tissue curves.

8. 3TP parameters were calculated for each tissue curve. The three time points were obtained by selecting a precontrast frame, and the first frame at least 2 minutes and 6 minutes after the contrast injection. Colors and intensities for each curve were assigned as described above.

Figure 5.2 displays representative tissue curves from the above simulations. Following the simulations, the root mean squared error (RMSE) of the estimated parameters was calculated. The errors were collected over all the simulated tumors and average RMSE values for each temporal resolution were calculated.

5.2.4 Clinical Data

The 3TP and ETK models were also applied to previously acquired breast DCE-MRI data from 87 patients. These data were collected as part of a prospective study on pharmacokinetic modeling in breast DCE [**?**]. All data was acquired on a 1.5 T Siemens Avanto scanner. The dynamic imaging was performed with 9.2-19.7 second temporal resolution using a fast 3D SPGR sequence (TR/TE/alpha = 2.54/1.09/10) with 1.5 mm isotropic resolution. Twenty-four of the datasets had a temporal resolution less than or equal to 12 seconds. Forty-two of the datasets had temporal sampling rates between 12 and 16 seconds, and 21 of the datasets

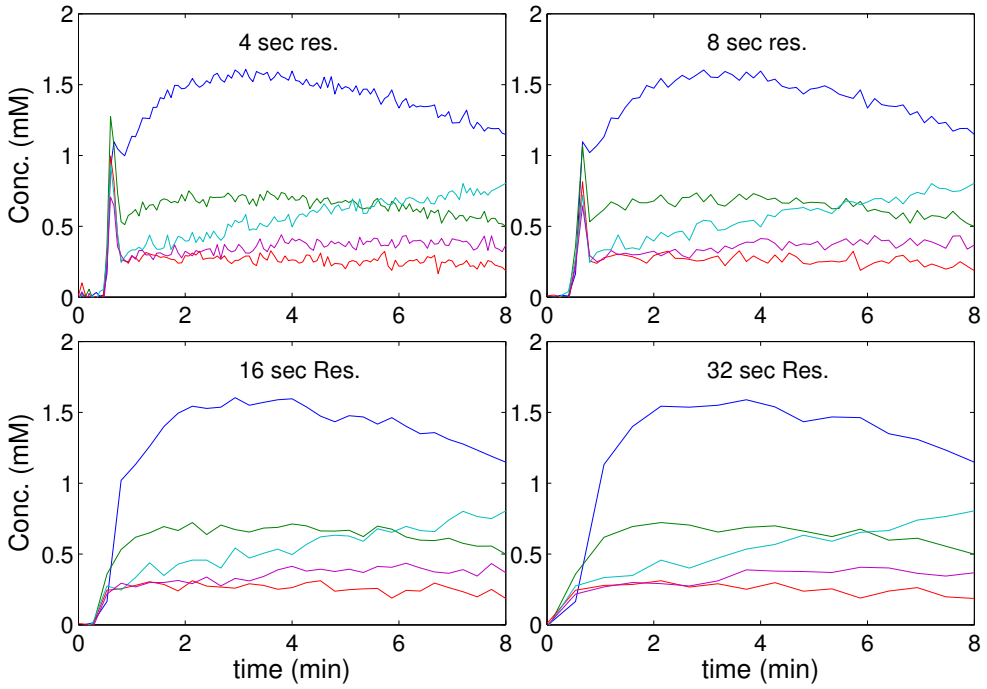

Figure 5.2. Sample tissue curves from temporal resolution simulations. Each set of curves was created from kinetic parameters derived from previously acquired patient data. The tissue curves were created with 1 second temporal sampling and Gaussian white noise (σ=0.03 mM) was added. The curves were then downsampled to 4, 8 16 and 32 second resolution.

had a sampling rate above 16 seconds. Partial Fourier encoding in the phase and frequency encoding directions was used and full bilateral coverage from the chest wall to the nipple was obtained in all scans. A 20 mL injection of gadodiamide (Omniscan, Amersham Health) was given at a rate of 4 mL/s, followed by a 20 mL saline flush at 2 mL/s. Eight to 10 minutes of data was acquired. Each of the datasets was downsampled temporally by selecting every second time frame and every fourth time frame to obtain datasets with temporal sampling rates ranging from 18.4-39.4 and 36.8-78.8 seconds/frame.

Each of the subjects in the previously referenced study had been referred to biopsy independent of any MRI results. All imaging results were correlated with pathology. In addition, following data acquisition, one region of interest (ROI) per patient was identified in each subject by an experienced observer.

Pharmacokinetic parameters were calculated for each voxel within the defined ROIs. The AMM estimated AIF was used and separate calculations were done for both the original and two downsampled datasets. For the AMM method, all of the tissue curves within the ROI were used as input. These curves were clustered using an unsupervised k-means algorithm, and the cluster averaged curves were used as input to the AMM algorithm. A population average AIF, based on that reported by Parker et al. [**?**], was used to initialize the algorithm. As with the simulations above, the tissue curves were upsampled to 1 second resolution with cubic interpolation, and the AIF was estimated on a 1 second resolution grid. This AIF was then used to estimate kinetic parameters voxelwise throughout the field of view. Following parameter calculation, mean values for each of the parameters were found for each region of interest. Parameters were also calculated for each voxel using the 3TP model described above.

Following parameter calculation, each of the lesions was classified as either benign or malignant. Classification of lesions with the 3TP parameters was done using the method outlined in [**?**], which distinguishes lesions based on the percentage of voxels assigned red. When a lesion has 15% or more red voxels, it is likely malignant. When the number of red voxels is less than 10%, the lesion is likely benign. For intermediate lesions, a second 3TP analysis with time points at 4 and 8 minutes after injection is

done and the lesion is reclassified.

For the ETK parameters, lesions were classified with linear combinations of parameters. Each of the possible linear combinations of parameters (i.e., K^{trans}, k_{ep}, v_p, K^{trans}/k_{ep}, K^{trans}/v_p, k_{ep}/v_p, $K^{trans}/k_{ep}/v_p$) was considered as a possible classifier. Parameters were combined using the method outlined in [**?**]. This was repeated for each patient in a leave one out manner with a possible unique classifier for each dataset. A standard method [**?**] was used to calculate the ROC curves for each combination. Separate ROC curves were generated using the original data and each set of downsampled data.

Classification of the lesions for both the 3TP and ETK parameters was also done retrospectively, to find the optimal linear combination of parameters that maximizes the area under the ROC curve (AUC). As with the classification for the ETK method above, each of the possible linear combinations of the parameters was tested (i.e. red, green, blue, red/green, red/blue, green/blue, red/green/blue). The intensities of the colors assigned to the voxels were used to classify the lesions. All of the lesions were included in the analysis, and the optimal linear classifier was found for both the 3TP and ETK parameters for each temporal resolution.

5.3 Results

5.3.1 Temporal Resolution Simulations

Aggregate results from all 75 simulated lesions are seen in Figure 5.3. This figure displays the average RMS error ($\pm$1 SD) for the simulations at each temporal resolution, for each parameter. The error in the ETK model with the AMM estimated AIF increases linearly with the temporal resolution of the input curves. The RMSE increases by approximately 70% when the temporal sampling rate increases from 4 to 32 seconds. The RMS errors in the parameters from the 3TP method remained constant as the temporal sampling changed. These errors were largely due to incorrect binning of the voxels as the temporal resolution changed.

5.3.2 Clinical Data

Figure 5.4 displays modeling results from a representative slice from one of the lesions in this study. The first panel shows K^{trans} values calculated with an AMM

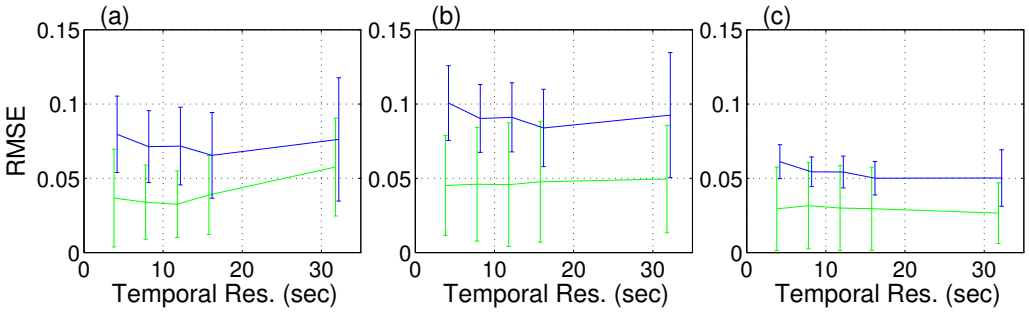

Figure 5.3. The average RMS error for each parameter for all of the temporal sampling simulations. Panel (a) corresponds to K^{trans}/red, (b) to k_{ep}/green, (c) to v_p/blue. In each panel, the green curve corresponds to ETK parameters with an AMM estimated AIF, and the blue curve to 3TP parameters.

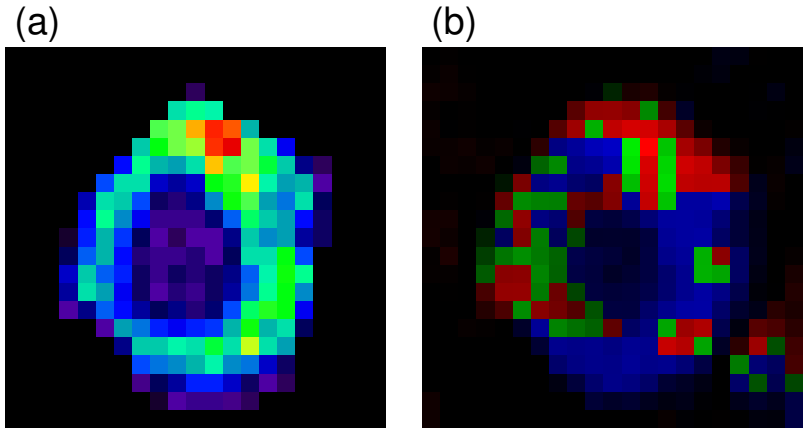

Figure 5.4. Parameter maps from a representative slice of DCE-MRI data taken from the left breast of a patient with infiltrating ductal carcinoma. Panel (a) corresponds to K^{trans} values calculated with an AMM estimated AIF and (b) to 3TP parameters.

estimated AIF. The second panel displays the 3TP parameters for the same slice. These parameters were from a subject with pathology proven IDC, and the elevated K^{trans} values seen here are consistent with literature reports [**?**].

ROC curves for the 3TP method using a prospective classifier are plotted in Figure 5.5. For each of the lesions defined in this study, diagnoses were obtained from MRI independent pathology reports. Of the lesions studied here, 25 were classified as

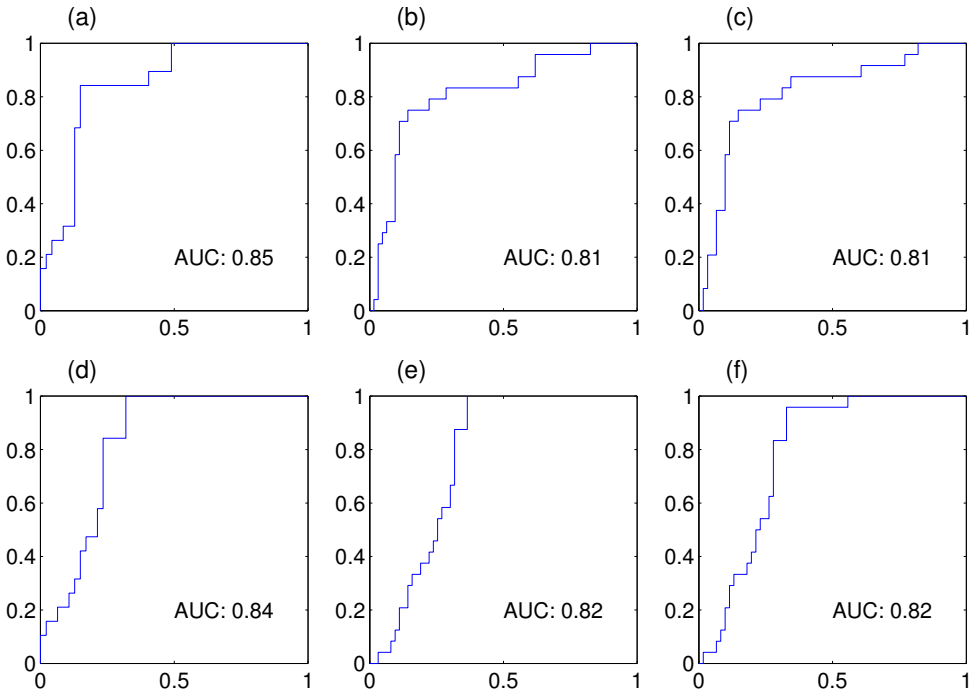

Figure 5.5. ROC curves for the 3TP method using a literature (prospective) classifier as well as those for the ETK method using a leave-one-out analysis. The first row displays ROC curves for the 3TP method with the original dataset (a), for the data downsampled by a factor of 2 (b), and 4 (c). The second row corresponds to the ETK method with the original data (d), as well as the downsampled datasets (e) and (f). The area under the ROC curve is indicated on each plot.

malignant. The remaining 62 lesions were defined as benign. Using the classifier for the 3TP parameters, the AUC was 0.85, with a 95% confidence interval (CI) of 0.74-0.96. When the data were temporally downsampled by a factor of two prior to parameter calculation, the AUC of the ROC curve decreased to 0.81 (CI:0.70-0.92). When the data were downsampled by a factor of 4, the 3TP classifier was unchanged, with an AUC of 0.81 (CI:0.70-0.92). ROC curves for the ETK method are also shown in Figure 5.5. These curves were generated using a leave-one-out analysis. At the native resolution of the scans, the AUC of the ROC curve was 0.85 (CI:0.72-0.96). When the data were downsampled by a factor of 2, the AUC decreased to 0.82 (CI:0.71-0.93). When the data were further downsampled, the AUC remained 0.82 (CI:0.70-0.93).

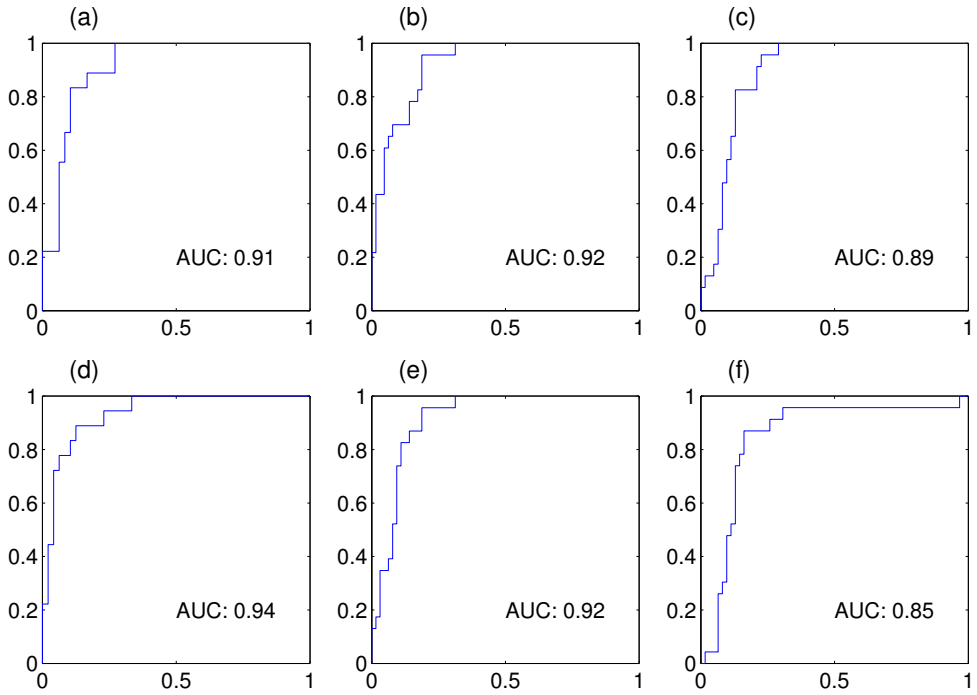

Figure 5.6. ROC curves for both the 3TP and ETK methods using a retrospectively determined classifier. The first row displays ROC curves for the 3TP method with the original dataset (a), for the data downsampled by a factor of 2 (b), and 4 (c). The second row corresponds to the ETK method with the original data (d), as well as the downsampled datasets (e) and (f). The area under the ROC curve is indicated on each plot.

When the optimal linear classifier was found retrospectively, the AUC for the 3TP increased. The ROC curves for both the 3TP and ETK methods with a retrospective classifier are seen in Figure 5.6. The first row corresponds to values from the 3TP method, and the second row to the ETK analysis. For the original dataset, with temporal sampling rates ranging from 9.2-19.7 seconds, the 3TP method AUC was 0.91 (CI:0.82-1.00) and the ETK method AUC was 0.94 (CI:0.86-1.00). When the data was downsampled by a factor of 2, the 3TP AUC increased to 0.92 (CI:0.85-1.00) and the ETK method decreased to 0.92 (CI:0.84-0.99). When the data was downsampled by a factor of 4, the 3TP AUC decreased to 0.89 (CI:0.81-0.98) and the ETK method decreased to 0.85 (CI:0.74-0.95).

5.4 Discussion

This chapter presents results comparing the semiquantitative three-time-point method and the fully quantitative extended Tofts-Kety compartmental modeling method for evaluating breast DCE-MRI. Semiquantitative models, such as the three time point method studied here, return parameters that are dependent on the overall shape of the tissue curves, and thus reflect tissue physiology only indirectly. As shown in the simulations carried out here, the accuracy of the 3TP method is insensitive to the temporal sampling rate of the acquired data. As a result, the analysis can be done with higher spatial resolution images in conjunction with morphological assessments [**?**]. In addition, the computational load of the 3TP method is minimal compared to the quantitative methods.

The parameters of fully quantitative models, such as the K^{trans}, k_{ep}, v_p, and v_e parameters in the extended Tofts-Kety model, directly reflect tissue physiology. They can provide insight into the makeup of the tissue and have been shown to correlate well with pathology [**?**], although other models have also been proposed [**?**]. Quantitative modeling has also been shown to track treatment response in various chemotherapies in longitudinal studies.

The AIF model implemented here was the AIF estimated with the alternating minimization with model algorithm. This algorithm attempts to find an input function that best fits the tissue concentration data within the AIF and tissue response models. Estimating the input function allows for greater interpatient individuality than a population average input function. Also, the heterogeneity of the tissue curves in many breast lesions results in higher expected accuracy in the AIF estimation (see Chapter 3). The estimation can be done at high temporal resolution, allowing for fine structure not available at lower sampling rates. Despite the high resolution grid that can be used for the AIF estimation, the information available from the tissue curves will depend on the native sampling rate. Henderson reports that for curves with nonzero contribution from the blood plasma volume (v_p) and with a known AIF, the tissue curves must be sampled with at least four second resolution to obtain less than 10% error in all of the parameter estimates [**?**]. This same study reports that if errors in the plasma volume are ignored, the sampling rate can be relaxed to 16 seconds.

In comparison, Schabel reports results from simulations done with a Monte Carlo type estimation method for obtaining the AIF on the effect of the temporal sampling rate on the accuracy of the estimated kinetic parameters [**?**]. This method can be considered a generalization of the method employed here. These simulations return good estimates of all of the parameters at reasonable noise levels and at sampling rates up to 8 seconds, after which the errors grow rapidly with increasing sampling rates. The Monte Carlo method also found that, ignoring any errors in v_p, K^{trans} and k_{ep} estimates were stable up to sampling rates of twelve seconds, after which the error increase rapidly.

The fastest sampling rate in the clinical data studied here was more than twice as long as the 4 seconds recommended by Henderson, and more than one second faster than the 8 seconds reported by Schabel. As a result, voxels with nonzero v_p are not sampled sufficiently quickly, and much of that information is lost, even with high resolution AIF estimation. In lesions where v_p is small enough to be neglected, Henderson's recommendation for the required sampling increases to 16 seconds [**?**], while Schabel's recommendation increases to only 12 seconds [**?**]. In comparison, the temporal sampling rate of the data acquired here ranges up to 19.7 seconds. More work is needed to understand the relationship between nonzero v_p and the AIF estimation at nonoptimal temporal sampling rates.

Other method of estimating the AIF have been used in breast DCE-MRI analysis. Reference region approaches, such as those done by Yankeelov et al. [**?**, **?**], attempt to avoid the complications due to AIF uncertainty by calculating kinetic parameters through comparison of unknown tissue curves to reference curves with known tissue parameters. These methods do not require an AIF estimate, and have been shown to return kinetic parameter estimated comparable with AIF deconvolution approaches. The reference region method, which does not typically included v_p estimates, was shown in simulation to provide estimates of K^{trans} and k_{ep} with less than 10% error at temporal resolutions up to 29 seconds, after which the error begins to increase [**?**]. In these studies, the pectoral muscle is used as a reference region. Further validation of the reference region approach is still needed, as the reference tissue values may not be consistent across patients.

Some work has also been done measuring the AIF directly from arterial voxels within the imaging field of view [**?**]. However, unless a variable sampling rate acquisition is used, measured AIFs will have the same temporal sampling rate as the tissue enhancement curves. In addition, arteries adjacent to the breast tissue tend to be small with respect to the voxel size, and partial volume effects may affect the concentration measurements.

The ultimate utility of any analysis method is its diagnostic usefulness. The selection of an optimal linear classifier based on the analysis parameters remains an open question for both quantitative and semiquantitative analysis. As seen in Figure 5.5, the literature classifier used in conjunction with the 3TP method yields good results (i.e. $AUC > 0.8$) regardless of the temporal resolution, and is comparable to similar studies with other semiquantitative analysis methods [**?**]. As mentioned in [**?**], this classifier is often used in conjunction with radiologist interpretation of the images to arrive at a diagnosis. The leave-one-out method returned similar results using the ETK parameters, which suggests that a prospective classifier based on the ETK model may be clinically feasible at the temporal sampling rates studied here.

As with previous analyses of various diagnostic techniques [**?**, **?**], the pathology proven diagnoses allowed the selection of a retrospectively determined classifier for optimally distinguishing benign and malignant lesions. This was especially useful for the ETK analysis, where no consensus has been reached on how to classify lesions based on the estimated parameters. As seen in Figure 5.6, the optimal linear 3TP classifier outperforms the literature classifier for the 3TP method, as would be expected. This type of analysis is not typically used in conjunction with the 3TP parameters, but is included here to allow for direct comparison with the ETK method. The change in the optimal classifier performance, as measured by the AUC, is small as the temporal resolution of the data lengthens. This is due to the general insensitivity of the 3TP method to temporal sampling within the range of this study. The ETK method, on the other hand, is more sensitive to the temporal sampling of the acquired data. For the most rapidly sampled data the ETK method had the highest overall optimal performance. As the temporal sampling rate increased, the AUC of the ROC curves for the ETK method decreased more rapidly than those for

the 3TP method.

It should also be noted that the analysis performed here did not include any morphological assessment of the acquired data. The increased temporal sampling rate of the data used in this study led to a decrease in the acquired spatial resolution (1.5mm isotropic resolution here, compared to sub millimeter resolution obtained in more standard breast DCE-MRI scans). Morphological assessment, when combined with the semi-quantitative analyses studied here, may provide additional power in distinguishing lesions.

5.5 Conclusion

The AMM-estimated AIF was shown in simulation to return parameters with lower mean error than the 3TP method at all temporal sampling rates studied here. In addition, simulations showed that as the temporal sampling rate of the input data increased, the error in the parameters decreased. The leave one out analysis done with the ETK parameters performed as well as the conventional 3TP analysis across all temporal resolutions. When applied to clinical data acquired at 9-19 seconds per frame temporal resolution, the ETK analysis was able to distinguish benign and malignant lesions more accurately than the 3TP analysis when optimally determined classifiers were used. As the data were increasingly undersampled temporally, the ETK performance decreased to a level equal to that of the 3TP analysis. With further temporal undersampling, the ETK methods performance was worse than that for the 3TP method. As undersampling acquisition and reconstruction techniques improve, high temporal resolution acquisition of DCE-MRI data will become more realizable. The ability of the fully quantitative modeling to report on subject physiology may make it a more attractive analysis option than semiquantitative analyses, especially with no expected loss in distinguishing power relative to semiquantitative analyses.

CHAPTER 6

CONCLUSION

This dissertation focuses on the problem of properly identifying the arterial input function (AIF) for use in conjunction with compartmental modeling in quantitative DCE-MRI. The accuracy of the measured kinetic parameters depends on the AIF used in the model deconvolution.

6.1 Summary of Work

A novel method for extracting the AIF directly from the tissue curves was developed. This method makes use of a functional form for the AIF, which serves to reduce the impact of measurement noise, and to simplify the estimation process. The method minimizes a cost function based on the compartmental model by alternately refining the estimates for the kinetic and AIF model parameters. This alternating minimization with model (AMM) method is tested in simulation and compared to deconvolution approached with measured input functions. The method is also tested in *in vivo* datasets, each of which contain arterial voxels from which a measured AIF can be used for comparison. The shape of the AMM-estimated AIF is found to be strongly dependent on whether arterial voxels are used to constrain the estimation process, as well as the diversity of the kinetic parameters of the tissue curves input to the algorithm.

Based on the above observations, a metric was created to provide an estimate for the uncertainty in the AMM-derived AIF. This metric is a function of the SNR and heterogeneity of the tissue curves input to the algorithm. Using computer simulations, the error in the kinetic parameters estimated using the AIF from the AMM algorithm was found to decrease exponentially as the SNR of the input tissue curves increased. A similar exponential decline in error was seen as the heterogeneity

of the input tissue curves increased. The spread of the k_{ep} and v_p parameters in normalized parameter space was used as a measure of curve diversity.

This metric was used in *in vivo* data to estimate input functions within a small region of data (i.e., 10X10X10 voxels. These local input functions were then used to calculate kinetic parameters. When the local input functions were used in place of either globally estimated or measured AIFs, the kinetic parameters were significantly different.

The AMM algorithm was also adapted for use in cardiac applications. Unlike imaging in many other parts of the body, in myocardial imaging the signal in the blood pool is easily measurable. However, due to high concentrations of contrast agent in the blood pool, signal saturation can significantly affect the AIF measurement and resulting kinetic parameters. This signal saturation can be corrected to some degree using the signal equations for the image sequence used during acquisition. This corrected signal can in turn be used to constrain the alternating minimization. This constrained estimation was tested in both computer simulation and with *in vivo* datasets. In 85% of the datasets studied here, the K^{trans} values calculated with the estimated AIF were not significantly different from those found using the more conventional dual bolus method.

In most clinical breast DCE-MRI, a high emphasis is placed on acquiring high spatial resolution data, with a concomitant increase in the temporal sampling rate. The poor temporal resolution in breast scanning has made quantitative modeling difficult. The AMM algorithm was used in conjunction with clinical breast cancer data to obtain pharmacokinetic parameters. The effects of various temporal sampling rates on the quantitative modeling were examined with computer simulation and with *in vivo* data. The specificity and sensitivity of the AMM method parameters were compared with more conventional three-time-point analyses. Two different classifiers were used, and in both cases the sensitivity and specificity of the AMM parameters were not significantly different from the three-time-point diagnoses.

6.2 Future Work

As mentioned above, one drawback in analyzing the effectiveness of the AMM algorithm is the difficulty in ascertaining absolute truth in *in vivo* data for comparison. The parameters of the compartment model quantify physiology in a way that is difficult to assess with histology. However, histological examination of tissues, for example with animal models, can correlate with the measured parameters and provide some measure for the accuracy of these parameters. Future work may focus on validating the AMM algorithm through histological analysis of animal model data.

In addition, the efficacy of local input functions (as described in Chapter 3) in discriminating disease or monitoring treatment should be investigated. Locally estimated input functions have the potential to improve compartmental model fidelity, particularly in large heterogeneous tumors. Large tumors often have necrotic cores with a very different blood supply than the actively growing rim. Adapting the AIF to match the tissue curves in different regions of the tumor may result in more accurate parameter estimation. The downstream utility of this increased accuracy should be investigated.

Chapter 4 describes a method for constraining the AMM estimation by using the measured blood pool signal from the left ventricle. The model also implements signal saturation correction based on the signal equations for the acquisition sequence. The constraint used in this implementation was fairly simple, with a binary correction for signal saturation. Also, only a single value for the weight of the constraint was tested. Further work in refining both the concentration estimation and weighting the blood pool constraint is needed.

In Chapter 5, it was shown that the AMM method is able to distinguish benign and malignant lesions at nearly the same rate as the three-time-point method, even at low temporal sampling rates. The AMM method is also able to provide physiological measures for the tumor, which may be beneficial in longitudinal studies tracking treatment response. Further work is needed to determine what benefits parameter estimation may bring.